Designer magnetoplasmonics for adaptive nano-optics

THESIS FOR THE DEGREE OF DOCTOR OF PHYLOSOPHY IN

NATURAL SCIENCE

Designer magnetoplasmonics for adaptive nano-optics

Irina Zubritskaya

UNIVERSITY OF GOTHENBURG

THESIS FOR THE DEGREE OF DOCTOR OF PHYLOSOPHY IN NATURAL SCIENCE

Designer magnetoplasmonics for adaptive nano-optics

Irina Zubritskaya

ISBN 978-91-629-0255-1 (Print)

ISBN 978-91-629-0254-4 (PDF)

Available online at http://hdl.handle.net/2077/53238

Department of Physics

UNIVERSITY OF GOTHENBURG

412 96 Göteborg
Sweden

Cover illustration:
Top left: Active magnetoplasmonic ruler built on nickel dimer nanoantennas
Top right: Transparent magneto-dielectric surface with chiroptical transmission built on hybrid trimer nanoantennas that are made of two silicon nanodisks and a magnetic multilayer nanodisk of cobalt and gold
Bottom: Chiroptical plasmonic surface with magnetically tunable chiral differential transmission built on trimer nanoantennas made of two gold and one nickel nanodisks

Printed by INEKO AB, Göteborg, 2017

Abstract

Materials that provide real-time control of the fundamental properties of light at visible and near-infrared frequencies enable the essential components for future optical devices. Metal nanostructures that couple electromagnetic (EM) radiation on a sub-wavelength length scale to free electrons, forming propagating or localized surface plasmons, provide many exciting functionalities due to their ability to manipulate light via the local EM field shaping and enhancement. Magnetoplasmonics is an emerging field within nano-optics that operates with the combination of propagating or localized surface plasmons and magnetism. Active and adaptive magnetoplasmonic components capable of controlling light on the nanoscale with externally applied magnetic fields are envisioned to push the development of integrated photonic circuits, high-density data storage, or the advanced schemes for bio- and chemo-sensing. In these components plasmon-enhanced and controlled magneto-optical activity creates a new way of control for plasmonic devices, which is explored in this thesis.

Another focus of this thesis are chiral plasmonic materials that exhibit an enhanced chiroptical response due to the nanoconfinement of light and strong near-field coupling. These have benefits in applications like chiral sensing. Fundamentally, they offer an additional degree of freedom to control the phase and polarization of light on the sub-wavelength scale via interaction with its helicity, i.e., angular momentum. Adaptive chiral materials provide a new pathway for real-time control of chiral light's scattering and absorption by weak magnetic fields. Engineering of chiral materials that can manipulate the helicity of light is decisive for angular momentum-controlled nanophotonics.

A general topic of this thesis is the design and fabrication of advanced optical nanoantennas, used to dynamically manipulate light. Among applications are nanorulers, adaptive magneto-chiral and highly transparent magneto-dielectric surfaces.

Keywords: Photonics, magnetoplasmonics, magneto-optics, magneto-optical Kerr effect (MOKE), plasmon ruler, nickel, cobalt, gold, silicon, localized surface plasmon resonance, dimer, trimer, chiroptics, chiral transmission, 2D nanoantennas, dynamic tuning, metal-dielectric, 3D nanoantennas, metasurface, magnetic modulation, perpendicular magnetic anisotropy.

Publications

List of papers and manuscripts included in this thesis:

Paper 1: ***Magnetoplasmonic design rules for active magneto-optics.***
Lodewijks, K.; Maccaferri, N.; Pakizeh, T.; Dumas, R. K.; Zubritskaya, I.; Akerman, J.; Vavassori, P.; Dmitriev, A. *Nano Letters* **2014,** 14, (12), 7207-14.

I contributed to discussions and samples fabrication.

Paper 2: ***Active magnetoplasmonic ruler.***
Zubritskaya, I.; Lodewijks, K.; Maccaferri, N.; Mekonnen, A.; Dumas, R. K.; Åkerman, J.; Vavassori, P.; Dmitriev, A. *Nano Letters* **2015,** 15, (5), 3204-11.

I took part devising the concept, performed all nanofabrication, optical and MOKE experimental measurements. I wrote first version of the manuscript.

Paper 3: ***Magnetic control of the chiroptical plasmonic surfaces.***
Zubritskaya, I; Maccaferri, N; Inchausti Ezeiza, X; Vavassori, P; and Dmitriev, A. *Submitted.*

I took part devising the concept, performed all nanofabrication, measurements of circular differential transmission and magnetically tunable circular differential transmission. I wrote first version of the manuscript.

Paper 4: ***Transparent chiroptical magneto-dielectric surfaces.***
Zubritskaya, I; Maccaferri, N; Pedrueza Villialmanzo, E; Vavassori, P; and Dmitriev, A. *In manuscript.*

I took part devising the concept, performed all nanofabrication, optical measurements, measurements of magnetic hysteresis loops and circular differential transmission. I wrote first version of the manuscript.

Contents

“Nothing is too wonderful to be true, if it be consistent with the laws of nature”

Michael Faraday

1 Why magnetoplasmonics?

Surface plasmons are electromagnetic waves coupled to the collective oscillations of the free surface charges, strongly localized at an interface between two media with permittivities with opposite sign, typically a dielectric and a metal. They can exist either in the form of localized surface plasmons in nanoparticles, or as surface plasmon polaritons, also known as propagating plasmons, supported by planar interfaces. Plasmonics, being a major part of nanophotonics, is a research field that studies the phenomena and applications associated with surface plasmons [1-3], which was established around the turn of 20th century. *Magnetoplasmonics* is a relatively young but extensively growing field, which merges plasmonics and magnetism to devise conceptually new functionalities [4, 5]. The investigation of the phenomena arising from the mutual interplay of magnetism and light-matter interactions in spatially confined geometries became a hot topic owing to the recent advances in nanotechnology. The research route of magnetoplasmonics is twofold: controlling the plasmon properties with magnetic field on one hand and controlling the magneto-optical properties with plasmons on the other hand. The first route mainly focuses on the modulation of propagating surface plasmons with magnetic field. It was in early ’70s when the effect of magnetic field on plasmons was first analyzed on structures made of highly doped semiconductors and metals supporting propagating plasmons in far-infrared region. The idea to control the properties of plasmons, such as propagation and localization, became very appealing for the development of new active devices; however, too high magnetic fields, required for the proper control of the plasmon wave vector, hindered it from realization in real applications. Nanoengineering of new systems made from ferromagnetic materials and noble metals made it possible to control the plasmon wave vector with weak external magnetic field [6, 7] and generate ultrashort surface plasmon polariton pulses [8, 9]. Magnetic manipulation of propagating plasmons in magnetoplasmonic crystals, leading to the enhancement of magneto-optical activity and magneto-optical transparency [10], makes these systems suitable for applications in telecommunications, magnetic sensing and all-optical magnetic data storage. The recent review [11] highlights recent advances in the field of non-linear interactions in magneto- and acousto-plasmonic multilayers as well as non-linear magneto-plasmonics, and explains the role of the external magnetic field in

ultrafast magnetization dynamics and second harmonic generation in systems that support propagating plasmons. Another topic in magnetoplasmonics is the localized surface plasmons in purely magnetic or combined magnetic-noble metal systems. In contrast to heavily damped propagating plasmons in magnetic materials, localized plasmons have strong effects on magneto-optical activity due to the huge local field enhancement in spatially confined nanostructures. As a consequence, strongly enhanced magneto-optical activity [12] and tunability of magneto-optical response [13, 14] can be achieved with localized plasmons. Plasmon-enhanced and controlled magneto-optical activity creates a new way of active control of plasmonic devices by the weak magnetic fields. Because of that, magnetoplasmonic nanoparticles, or antennas, offer more flexibility than their non-magnetic counterparts, which has now been proved by their applications as rulers [15] and biosensors [16], non-reciprocal and one-way devices, and as contrast agents in magneto-photo-acoustic imaging [17]. Hybrid systems like core-shell particles, dumbbell-like dimers and cross-linked pairs based on magnetite and gold nanoparticles manifest an improved tunability, enhanced scattering efficiency and enhanced local field at the interface between magnetic and noble-metal components [18]. Recent report demonstrates a magnetic modulation of transmission approaching 100% by suspensions of superparamagnetic and plasmonic nanorod particles [19]. A further practical application, where magnetoplasmonics becomes eminent, is thermally-assisted magnetic recording, where the integration of a plasmonic antenna into a magnetic recording head shows to dramatically improve the storage density up to ~1 Tb/inch^2 [20].

In this thesis, I explore two routes leading to implementation of optical magnetoplasmonic nanoantennas as the future components in active and adaptive photonic devices that bring about a real-time control of light transmission, scattering and absorption by weak magnetic fields. The first route is realized through plasmon-enhanced and controlled magneto-optical activity and described in Paper 1 and Paper 2. The second route is tackled via magnetically manipulated interactions with light helicity in magneto-chiral antennas and discussed in Paper 3 and Paper 4.

2 Plasmonic nanoantennas

This chapter is focusing on plasmonics and describes the physics behind localized surface plasmon resonances in nanoparticles, making them antennas for light (nanoantennas). Antennas are electrical transducers that convert propagating electromagnetic waves (microwaves and radio frequency (RF) waves) into electric current or, radiate the electromagnetic waves from the current in a specific pattern. In direct analogy with low-frequency RF antennas, optical nanoantennas operate with light – electromagnetic waves in visible and near-infrared regions of the electromagnetic spectrum.

In section 2.1 I describe the optical properties of metals and provide the theoretical background of electromagnetics of metals in terms of classical electrodynamics based on Maxwell's equations. The role of dielectric function in optical properties of metals is explained. In section 2.2 I introduce localized plasmons in metal nanoparticles and provide the analytical expressions for the polarizability of sub-wavelength nanoparticles and also beyond the quasi-static approximation. I close this chapter by describing the effects of plasmon coupling on optical properties of nanoparticle dimers.

2.1 Optical properties of metals

The interaction of metals with electromagnetic fields is frequency-dependent. At microwave and far-infrared frequencies metals are highly reflective and do not allow the propagation of electromagnetic waves. The field penetration increases significantly at higher frequencies in near-infrared and visible parts of the spectrum. Electromagnetic fields with frequencies in ultraviolet region of the spectrum can penetrate into and propagate through the metals. Frequency-dependent character of optical response is closely related to the dispersive properties of the complex dielectric function $\varepsilon(\omega)$ and conductivity $\sigma(\omega)$.

2.1.1 Theoretical foundations of macroscopic electrodynamics

The optical properties of metals can be described in terms of classical electrodynamics based on Maxwell's equations. Maxwell's equations together with the Lorentz force law summarize the entire theoretical contest of classical electrodynamics and optics and tell how charges and currents generate fields and, reciprocally, how fields affect charges [21-23]:

$$\nabla \cdot E = \frac{1}{\varepsilon_0}\rho_{ext} \qquad (Gauss's\ law) \tag{1}$$

$$\nabla \cdot B = 0 \tag{2}$$

$$\nabla \times E = -\frac{\partial B}{\partial t} \qquad (Faraday's\ law) \tag{3}$$

$$\nabla \times B = \mu_0 J_{ext} + \mu_0 \varepsilon_0 \frac{\partial E}{\partial t} \qquad (Ampère's\ law\ with\ Maxwell's\ correction) \tag{4}$$

$$F = q\,(E + v \times B), \qquad (Lorentz\ force\ law) \tag{5}$$

where E denotes the electric field, B is the magnetic induction or magnetic flux density, J_{ext} and ρ_{ext} are the external current and charge densities, q is the electric charge, v is the velocity, ε_0 and μ_0 are the dielectric permittivity and the magnetic permeability of vacuum[1]. The continuity equation

$$\nabla \cdot J = -\frac{\partial \rho}{\partial t} \qquad (Continuity\ equation) \tag{6}$$

is the mathematical expression of conservation of charge and is built in Maxwell's equation. It can be derived by taking the divergence of Ampère's law [21],[22].

Constitutive relations display the material properties and show how it behaves under the influence of the fields. For non-dispersive linear[2] and isotropic[3] medium

[1] $\varepsilon_0 \approx 8.854 \times 10^{-12}\ F/m$ and $\mu_0 \approx 1.257 \times 10^{-6}\ H/m$

[2] In non-linear medium the polarization P is described by a Taylor series expansion and include the terms of higher power of E

[3] In anisotropic media ε and μ together with χ_e and χ_m are second-rank tensors: $\vec{\varepsilon} = \varepsilon_0(\tilde{I} + \vec{\chi_e})$ and $\vec{\mu} = \mu_0(\tilde{I} + \vec{\chi_m})$, $\tilde{I}$ is identity matrix

$$D = \varepsilon\varepsilon_0 E \qquad (P = \varepsilon_0 \chi_e\, E) \tag{7}$$

$$H = \frac{1}{\mu\mu_0} B \qquad (M = \chi_m H) \tag{8}$$

$$J = \sigma E, \tag{9}$$

where the dielectric displacement D, polarization P, the internal conduction current density J induced by the magnetization M, and the magnetic field H are expressed in terms of E and B with the conductivity σ and dielectric permittivity ε and magnetic permeability μ, which depend on the nature of the material and connected with electric and magnetic susceptibility χ_e and χ_m through the relations:

$$\varepsilon = \varepsilon_0(1 + \chi_e) \tag{10}$$

$$\mu = \mu_0(1 + \chi_m). \tag{11}$$

Importantly, Maxwell's and other equations in this section are written in their macroscopic form, which uses charge densities and current densities instead of total charge and total current. The microscopic properties of matter and microscopic fields can be included in Maxwell's equations by considering charges and currents at the atomic scale.

An electromagnetic time-dependent field in a linear medium can be written as a superposition of monochromatic plane-wave components [1, 22]

$$E(r,t) = E(k,\omega)\cos(k \cdot r - \omega t). \tag{12}$$

Therefore the induced dielectric displacement $D(r,t)$ and the internal conduction current $J(r,t)$ can be rewritten as [1, 22]

$$D(k,\omega) = \varepsilon_0 \varepsilon(k,\omega) E(k,\omega) \tag{13}$$

$$J(k,\omega) = \sigma(k,\omega) E(k,\omega), \tag{14}$$

were k and ω are the wavevector and the angular frequency. Since $E(k,\omega)$ is equivalent to the Fourier transform $\hat{E}$ of the time-dependent field $E(r,t)$, the inverse Fourier transform can be applied to equations (13) and (14) and the constitutive relations (7) and (9) can be rewritten in a general form taking into account the *non-locality* of the medium in time and space [22]:

$$D(r,t) = \varepsilon_0 \iint \tilde{\varepsilon}(r-r',t-t')E(r',t')dr'dt' \tag{15}$$

$$J_c(r,t) = \iint \tilde{\sigma}(r-r',t-t')E(r',t')dr'dt'. \tag{16}$$

In a *non-local* medium the displacement D and the conduction current J_c at time t depend on the electric field E at all times t' previous to time t, which referred to as *temporal dispersion*. Similarly, if the displacement D and the conduction current J_c at a point r depend on the electric field E at all neighboring points r', the medium is called *spatially dispersive* or *non-local*. While spatial dispersion is a very weak effect, the temporal dispersion is a widely encountered phenomenon and should be taken into account.

Spectral representation of time-dependent fields is given by Fourier transform and the spectrum $\hat{E}(r,\omega)$ of a time-dependent field $E(r,t)$ is defined as

$$\hat{E}(r,\omega) = \frac{1}{2\pi}\int_{\infty}^{-\infty} E(r,t)e^{i\omega t}dt. \tag{17}$$

The solution of Maxwell's equations in Fourier (frequency) domain $\hat{E}(r,\omega)$ can be found by applying Fourier transform to Maxwell's equations in time domain and making a substitution $\frac{\partial}{\partial t} \to -i\omega$. Together with constitutive relations (7) and (8) the substitution Maxwell's equations in Fourier domain will have a form:

$$\nabla \cdot \hat{D}(r,\omega) = \hat{\rho}_{ext}(r,\omega) \tag{18}$$

$$\nabla \cdot \hat{B}(r,\omega) = 0 \tag{19}$$

$$\nabla \times \hat{E}(r,\omega) = i\omega\hat{B}(r,\omega) \tag{20}$$

$$\nabla \times \hat{H}(r,\omega) = \hat{J}_{ext}(r,\omega) - \omega\hat{D}(r,\omega), \tag{21}$$

where the solution $\hat{E}(r,\omega)$ in frequency domain and the solution $E(r,t)$ in time domain are related through the inverse Fourier transform as

$$\hat{E}(r,t) = \int_{\infty}^{-\infty} \hat{E}(r,\omega) e^{-i\omega t} dt. \tag{22}$$

We rewrite the equations (13) and (14) by replacing $D(k,\omega)$ and $J(k,\omega)$ with $D = \varepsilon_0 E + P$ and $J = \frac{\partial P}{\partial t}$, where the latter comes from the relationships $\nabla \cdot P = -\rho$ and the conservation of charge $\nabla \cdot J = -\frac{\partial \rho}{\partial t}$:

$$\varepsilon_0 E(k,\omega) + P = \varepsilon_0 \varepsilon(k,\omega) E(k,\omega) \tag{23}$$

$$\frac{\partial P}{\partial t} = \sigma(k,\omega) E(k,\omega). \tag{24}$$

Finally, the fundamental relationship between the dielectric permittivity (dielectric function) $\varepsilon(k,\omega)$ and the conductivity $\sigma(k,\omega)$ can be found by making a replacement $\frac{\partial}{\partial t} \to -i\omega$ and expressing $\varepsilon(k,\omega)$ through $\sigma(k,\omega)$ [1]:

$$\varepsilon(k,\omega) = 1 + \frac{i\sigma(k,\omega)}{\varepsilon_0 \omega}. \tag{25}$$

This relationship can be simplified by assuming that ε is only the function of the frequency and not the wavevector, i.e. $\varepsilon(k=0,\omega) = \varepsilon(\omega)$, which is true for up to ultraviolet frequencies [1]:

$$\varepsilon(\omega) = 1 + \frac{i\sigma(\omega)}{\varepsilon_0 \omega}. \tag{26}$$

Both the dielectric function

$$\varepsilon(\omega) = \varepsilon_1 + i\varepsilon_2$$

and the conductivity

$$\sigma(\omega) = \sigma_1 + i\sigma_2$$

have their real and imaginary parts and are complex functions of the frequency ω. The optical properties of metals are described by the complex dielectric function $\varepsilon(\omega)$ with imaginary part $\varepsilon_2(\omega)$ that is responsible for light absorption and energy dissipation associated with the motion of free electrons in metals.

2.1.2 Dielectric function of metals

Plasma model can be used over a wide range of frequencies to describe the optical properties of metals. According to the free-electron model, free conduction electrons oscillate against the fixed ion lattice 180° out of phase relative to the driving electromagnetic field. The motion of free electrons is damped via collisions that occur with characteristic collision frequency $\gamma = {}^{1}/_{\tau}$, where τ is relaxation time of free electron gas. At room temperature $\tau \sim 10^{-14}$, which results in $\gamma \sim 100$ THz. According to Drude-Sommerfeld theory, the equation of motion of a free electron with mass m and charge e in external electric field E can be written as [1]

$$m\ddot{x} + m\gamma\dot{x} = -eE. \tag{1}$$

For harmonic time dependence of the driving field $E(t) = E_0 e^{-i\omega t}$ a particular solution of the equation describing the oscillation of the electron $x(t) = x_0 e^{-i\omega t}$ is used to find that

$$x(t) = \frac{e}{m(\omega^2 - i\gamma\omega)} E(t). \tag{2}$$

The displaced electrons of density n contribute to a macroscopic polarization $P = -nex$, or

$$P(t) = -\frac{ne^2}{m(\omega^2 - i\gamma\omega)} E(t). \tag{3}$$

We insert this expression into $D = \varepsilon_0 E + P$ and obtain that

$$D = \varepsilon_0 \left(1 - \frac{\omega_p^2}{\omega^2 + i\gamma\omega}\right) E, \tag{4}$$

where

$$\omega_p^2 = \frac{ne^2}{\varepsilon_0 m}$$

is the *plasma frequency* of the free-electron gas. Since $D = \varepsilon\varepsilon_0 E$, the dielectric function of the free electron gas is given by:

$$\varepsilon(\omega) = 1 - \frac{\omega_p^2}{\omega^2 + i\gamma\omega}. \tag{5}$$

The complex dielectric function ε consists of real and imaginary parts:

$$\varepsilon_1(\omega) = 1 - \frac{\omega_p^2 \tau^2}{1 + \omega^2 \tau^2} \tag{6}$$

$$\varepsilon_2(\omega) = 1 - \frac{\omega_p^2 \tau}{\omega(1 + \omega^2 \tau^2)}, \tag{7}$$

where $\gamma = {}^{1}/_{\tau}$ indicates damping due to the collisions. For large frequencies close to ω_p, the product $\omega\tau \gg 1$ resulting in predominantly real dielectric function

$$\varepsilon(\omega) = 1 - \frac{\omega_p^2}{\omega^2}, \tag{8}$$

which is known as the dielectric function of undamped free electron plasma [1]. In reality the optical response of noble metals (e.g. Au, Ag, Cu) in frequency region $\omega > \omega_p$ is highly affected by interband transitions, which are not included in Drude-Sommerfeld model and will be discussed in the next section. In low frequency regime, $\omega \ll \tau^{-1}$ which results in $\varepsilon_2(\omega) \gg \varepsilon_1(\omega)$ and metals are mainly absorbing [1].

2.1.3 Interband transitions in noble metals

At visible and higher frequencies the optical response of noble metals is determined by the transitions between the electronic bands. Interband transitions occur if photon energy exceeds the bandgap energy and bound electrons from lower-lying bands get into the conduction band. The dielectric function of interband transitions describing the contribution of bound electrons is given by [22]:

$$\varepsilon_{Interband}(\omega) = 1 + \frac{\tilde{\omega}_p^2}{(\omega_0^2 - \omega^2) - i\gamma\omega}, \tag{1}$$

where γ describes radiative damping in case of bound electrons. Here the frequency

$$\tilde{\omega}_p = \sqrt{\frac{\tilde{n}e^2}{m\varepsilon_0}}$$

has a different physical meaning than plasma frequency in plasma model with $\tilde{n}$ and m being the density and the effective mass of the bound electrons, and

$$\omega_0 = \sqrt{\frac{\alpha}{m}},$$

where α is the spring constant of the potential which keeps the electrons tied to the ion cores.

For visible and higher frequencies, the imaginary part of this dielectric function $\varepsilon_{Interband}(\omega)$ does not follow the Drude-Sommerfeld model in noble metals and resonantly increases due to interband transitions, which results in strong absorption [24]. As an alternative, the optical response of real metals in the frequency region $\omega > \omega_p$ can be described by a dielectric function, which accounts for the effect of all higher-energy interband transitions via a constant offset ε_∞ and given by:

$$\varepsilon(\omega) = \varepsilon_\infty - \frac{\omega_p^2}{\omega^2 + i\gamma\omega}. \quad (2)$$

The dielectric constant ε_∞ (usually $1 \leq \varepsilon_\infty \leq 10$) describes highly polarized environment created by the filled *d* band located close to the Fermi level [1].

2.2 Localized surface plasmons

Localized surface plasmons are collective oscillations of free electrons in metallic nanostructures at the interface between a metal and a dielectric. According to the simple Drude model, the electron cloud of free conduction electrons oscillates 180° out of phase relative to the driving electric field (Fig. 2.1c). The effective restoring force, originating from the positively charged ion lattice, is exerted on the conduction electrons so that a resonance can arise, leading to field enhancement both inside and in the near-field zone outside the particle [1].

Resonantly enhanced absorption and scattering in gold and silver nanoparticles falls into the visible region of the electromagnetic spectrum, which explains bright colors observed in transmitted and reflected light. This phenomenon found applications in the staining of glass for windows (Fig.2.1a) and ornamental cups two thousand years ago (Fig.2.1b) but did not have a clear explanation for a long time. Now we know that the colors are due to the interplay of absorption and scattering in nanometer-sized gold particles embedded in glass [1, 22]. Michael Faraday was the first in history to study the interactions of light and matter in the mid 1850s. For his experiments, he prepared several hundred transparent thin gold slides and shined light through them. To make the films thin enough to be transparent, Faraday used a chemical process that involved washing of the films, which Faraday noticed produced a faint ruby color fluid. He kept the samples of the fluids in bottles and when he was shining a beam of light through the liquid in 1856, Faraday observed that the light was scattered due to the presence of suspended gold particles that were too small to be observed with scientific apparatus of the time. Remarkably, after more than 150 years the Faraday's colloids are still optically active (Figure 2.1 d), when most of the colloidal solutions nowadays last for only few months and eventually aggregate and/or produce sediments. Because Faraday's bottles can't be unsealed without being damaged, it will remain a mystery.

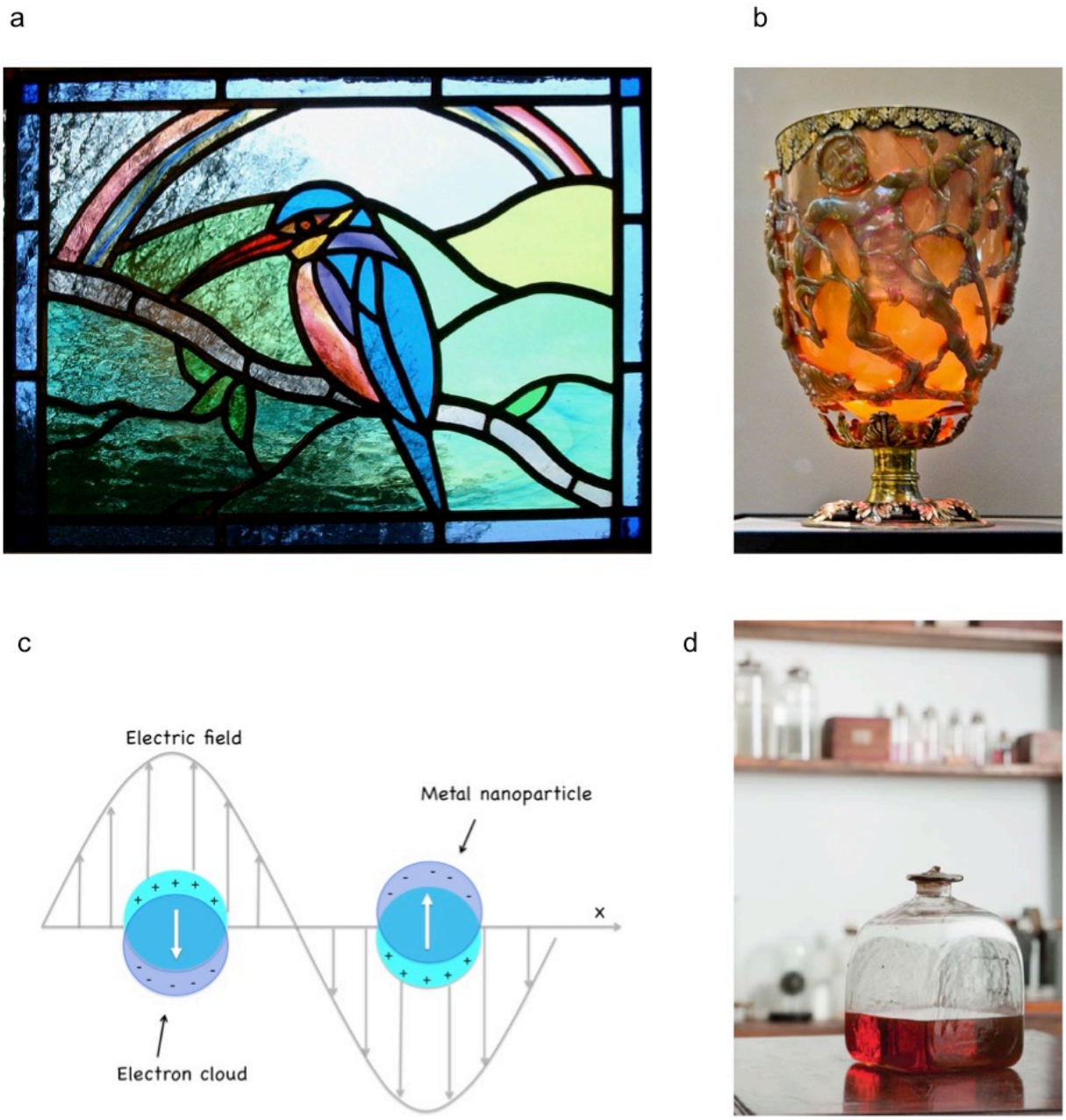

Figure 2.1. a) Kingfisher stained glass window, Worcester, UK. b) The Lycurgus Cup, 1700 years old. c) Illustration of dipole polarizability and oscillations of free electron density during localized plasmon resonance in metal nanoparticle. d) Gold colloids prepared by Michael Faraday more than 150 years ago, The Royal Institution of Great Britain, UK.

2.2.1 Polarizability of a sub-wavelength metal nanoparticle

To analyze the interaction of a particle of size d with electromagnetic field one assumes that the size of the particle d is much smaller that the wavelength of light $d \ll \lambda$, and

harmonically oscillating electric field $E(\omega) = E_0 e^{-i\omega t}$ is constant over the particle volume. This approach is known as *quasi-static approximation* and describes well the optical response of nanoparticles of dimensions around 100 nm and below. The harmonic time dependence $e^{-i\omega t}$ is added later when the field distribution is found. When a homogeneous metallic sphere of radius a is placed into a uniform electrostatic field (Fig. 2.2), the field induces a dipole moment inside the sphere, which is given by [1, 22]

$$p = 4\pi\varepsilon_0\varepsilon_m a^3 \frac{\varepsilon - \varepsilon_m}{\varepsilon + 2\varepsilon_m} E_0, \tag{1}$$

where ε and ε_m are the dielectric constants of the particle and the surrounding medium, E_0 is the amplitude of the external electric field.

The polarizability α of a metallic sphere in quasi-static approximation is defined via

$$p = \varepsilon_0\varepsilon_m\alpha E_0 \tag{2}$$

and given by

$$\alpha = 4\pi a^3 \frac{\varepsilon - \varepsilon_m}{\varepsilon + 2\varepsilon_m}. \tag{3}$$

It is clear that the polarizability in (3) experiences a resonant enhancement when $|\varepsilon + 2\varepsilon_m|$ is minimal, which in the case of small or slowly-varying $Im[\varepsilon(\omega)]$ simplifies to [1]

$$Re[\varepsilon(\omega)] = -2\varepsilon_m. \tag{4}$$

The relationship (4) is called the Fröhlich criterion and describes a *dipole surface plasmon* mode of the metal nanoparticle in a harmonically oscillating electric field $E(\omega) = E_0 e^{-i\omega t}$. For a sphere consisted of Drude metal with a dielectric function

$$\varepsilon(\omega) = 1 - \frac{\omega_p^2}{\omega^2 + i\gamma\omega},$$

located in air, the Fröhlich criterion is met at $\omega_0 = {}^{\omega_p}/_{\sqrt{3}}$. The resonance frequency ω_0 depends on the dielectric constant of the surrounding medium ε_m and the resonance redshifts as ε_m increases. Based on that fact, metal nanoparticles are perfectly suited for optical

sensing of changes in refractive index [1].

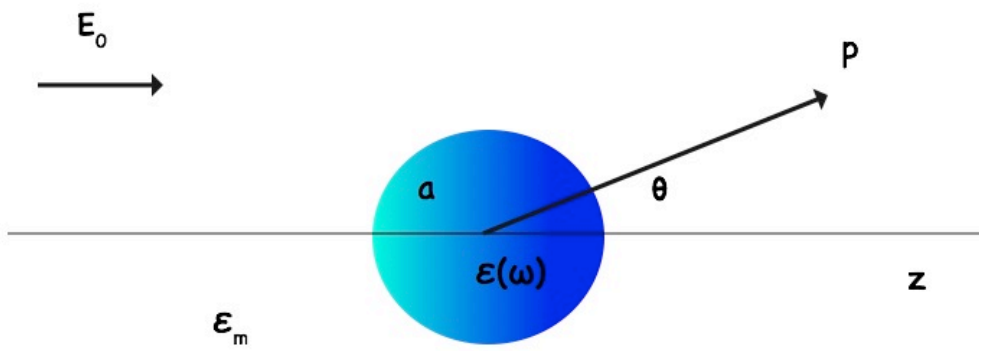

Figure 2.2. Schematics of a metal sphere in the electrostatic field E_0.

For harmonically oscillating electric field which excites a dipole moment $p(t) = \varepsilon_0 \varepsilon_m \alpha E_0 e^{-i\omega t}$ the polarizability is given by the same expression (3) as in quasi-electrostatic approximation. A metal nanoparticle of spherical shape at its plasmon resonance can be seen as a point dipole located in the center of the sphere. The radiation of this dipole leads to re-radiation and dissipation of the electromagnetic plane wave by the sphere [22], known as scattering and absorption, with corresponding scattering and absorption cross-sections given by [1]:

$$C_{sca} = \frac{k^4}{6\pi}|\alpha|^2 = \frac{8\pi}{3}k^4 a^6 \left|\frac{\varepsilon - \varepsilon_m}{\varepsilon + 2\varepsilon_m}\right|^2 \quad (5)$$

$$C_{abs} = kIm[\alpha] = 4\pi k a^3 Im\left[\frac{\varepsilon - \varepsilon_m}{\varepsilon + 2\varepsilon_m}\right]. \quad (6)$$

The important consequence of resonantly enhanced polarizability of a sub-wavelength metal nanoparticle, acting as an electric dipole, is that the nanoparticle resonantly absorbs and scatters electromagnetic fields at the dipole plasmon resonance. Extinction, being the sum of absorption and scattering, depends on the particle size (Fig. 2.3), shape and the dielectric function of the surrounding medium.

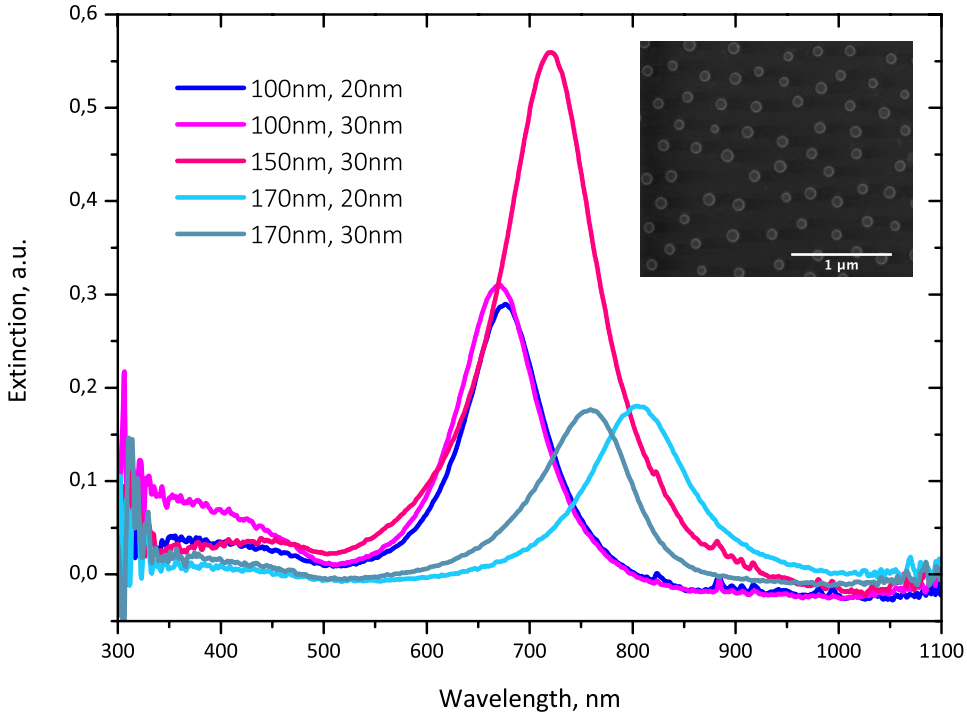

Figure 2.3. Extinction measured at around localized surface plasmon resonance in gold nanodisks with diameters 100, 150, 170 nm and thicknesses 20 and 30 nm fabricated with hole-mask colloidal lithography. Inset: SEM micrograph of nanodisks with diameter 150 nm.

Although the basic physics of localized surface plasmon resonance is described on the assumption of spherical shape of the nanoparticle, the polarizability can be derived for nanoparticles with more general ellipsoidal shape and is given by [1, 25]

$$\alpha_i = 4\pi a_1 a_2 a_3 \frac{\varepsilon(\omega) - \varepsilon_m}{3\varepsilon_m + 3L_i(\varepsilon(\omega) - \varepsilon_m)}, \tag{7}$$

where the semiaxes $a_1 \leq a_2 \leq a_3$ are specified by

$$\frac{x^2}{a_1^2} + \frac{y^2}{a_2^2} + \frac{z^2}{a_3^2} = 1.$$

α_i $(i = 1,2,3)$ define the polarizabilities along the principal axes of the ellipsoid. L_i are elements defined by the geometry and given by

$$L_i = \frac{a_1 a_2 a_3}{2} \int_0^\infty \frac{dq}{(a_i^2 + q) f(q)}, \tag{8}$$

where $f(q) = \sqrt{(q + a_1^2)(q + a_2^2)(q + a_3^2)}$. The elements L_i satisfy the condition $\sum L_i = 1$, and for a sphere $L_1 = L_2 = L_3 = {}^1\!/_3$. Alternatively, the polarizability of ellipsoids can be expressed in terms of *depolarization factors* $\widetilde{L_\iota}$, defined via $E_{1i} = E_{0i} - \widetilde{L_\iota} P_{1i}$, where $E_{1i}$and P_{1i} are the electric field and polarization induced inside the particle by the external field E_{0i} along the principal axis i. L_i and $\widetilde{L_\iota}$ are connected by the relationship

$$\widetilde{L_\iota} = \frac{\varepsilon - \varepsilon_m}{\varepsilon - 1} \frac{L_i}{\varepsilon_0 \varepsilon_m}. \tag{9}$$

Nanoparticles used in this work can be classified as a special case of ellipsoids with two major axes of the same size $a_1 = a_2$, called *oblate spheroids*. Nanoparticles of this shape exhibit two spectrally separated plasmon resonances corresponded to the oscillations of the conduction electrons along the major or the minor axes, respectively. The resonance along the major axis is significantly red-shifted compared to the resonance of a sphere of the same volume [1].

An important class of nanoparticles, which recently gained a great amount of attention in plasmonics due to their wide tunability of the resonance, is core-shell nanoparticles. The polarizability of a core-shell nanoparticle consisting of a dielectric core with $\varepsilon_1(\omega)$ and a metallic shell with $\varepsilon_2(\omega)$ is given by [25]

$$\alpha = 4\pi a_2^3 \frac{(\varepsilon_2 - \varepsilon_m)(\varepsilon_1 + 2\varepsilon_2) + f(\varepsilon_1 - \varepsilon_2)(\varepsilon_m + 2\varepsilon_2)}{(\varepsilon_2 + 2\varepsilon_m)(\varepsilon_1 + 2\varepsilon_m) + f(2\varepsilon_2 - 2\varepsilon_m)(\varepsilon_1 - \varepsilon_2)}, \tag{10}$$

where $f = {a_1^3}\!/_{a_2^3}$, a_1 and a_2 are the inner and the outer radii, respectively.

2.2.2 Plasmons beyond quasi-electrostatic limit

The results for resonantly enhanced polarizability, absorption and scattering by a sub-wavelength nanoparticle obtained in quasi-electrostatic approximation, where the nanoparticle is seen as an electric dipole, which absorbs and scatters light, is no longer valid for nanoparticles with dimensions compared to the wavelength of light. In practice,

the quasi-electrostatic approximation gives reasonably good results for spherical and ellipsoidal nanoparticles with dimensions below 100 nm, illuminated by visible or near-infrared light. For larger nanoparticles, where the driving electromagnetic field is not constant over the nanoparticle volume due to the phase-changes, one uses an approach known as *Mie theory* where internal and scattered fields are expanded into a set of *normal modes*. The expansion of the first TM mode of *Mie theory* gives an expression for the polarizability of a sphere with volume V, given by [1]:

$$\alpha_{Sphere} = \frac{1 - \left(\frac{1}{10}\right)(\varepsilon + \varepsilon_m)x^2 + O(x^4)}{\left(\frac{1}{3} + \frac{\varepsilon_m}{\varepsilon - \varepsilon_m}\right) - \frac{1}{30}(\varepsilon + 10\varepsilon_m)x^2 - i\frac{4\pi^2\varepsilon_m^{3/2}}{3}\frac{V}{\lambda_0^3} + O(x^4)}, \quad (1)$$

where $x = \frac{\pi a}{\lambda_0}$ is the *size parameter,* relating the radius a to the free-space wavelength. Formula for the polarizability (1) can be generalized for ellipsoid structures, giving the polarizability along the principal axis with geometrical factor L [1]:

$$\alpha_{Ellipsoid} \approx \frac{V}{\left(L + \frac{\varepsilon_m}{\varepsilon - \varepsilon_m}\right) + A\varepsilon_m x^2 + B\varepsilon_m^2 x^4 - i\frac{4\pi^2\varepsilon_m^{3/2}}{3}\frac{V}{\lambda_0^3}}, \quad (2)$$

where the parameters A and B are the functions of L and obtained using empirical data. The term quadratic in x in the numerator includes the effect of retardation of the exciting field over the volume of the sphere. Another quadratic term in the denominator describes the effect of the retardation of the *depolarization field* inside the particle. Both effects lead to a red-shift of the resonance as the size of the particle increases, which also means that the influence of the interband transitions gets limited as the resonance shifts towards lower energies. The imaginary term in the denominator accounts for *radiation damping,* caused by a direct radiative decay route of the coherent electron oscillations into photons [1].

There are two main mechanisms of plasmon damping beyond the electrostatic approximation in nanoparticles made of noble metals: a radiative decay into photons, dominating for larger particles, and non-radiative decay (absorption) due to thermalization or the creation of short-lived electron-hole pairs via either intraband or interband transitions [1]. In ferromagnetic nanoparticles, plasmons in addition are heavily

damped via thermal decay due to ohmic losses. Damping processes are responsible for a significant broadening of the plasmon resonance linewidth.

2.2.3 Plasmon coupling

The interaction between localized surface plasmon resonances of individual nanoparticles in complex structures, referred to as plasmon coupling, leads to the *hybridization* of individual plasmon modes [26]. In arrays of small nanoparticles, the electromagnetic interactions between the localized modes can in first approximation be treated as an interaction between point dipoles. This interaction is strongly dependent on the interparticle distance. For closely spaced particles with $d \ll \lambda$, near-field interactions with a distance dependence d^{-3} dominate, and the particle array can be seen as an array of point dipoles interacting via their near-field. Near-field coupling results in strongly enhanced local field in the nano-gaps between or at the intersection points of adjacent particles [1, 22], which decays as d^{-3} with distance (see Fig. 2.4). For larger particle separations, far-field dipolar coupling with a distance dependence d^{-1} dominates.

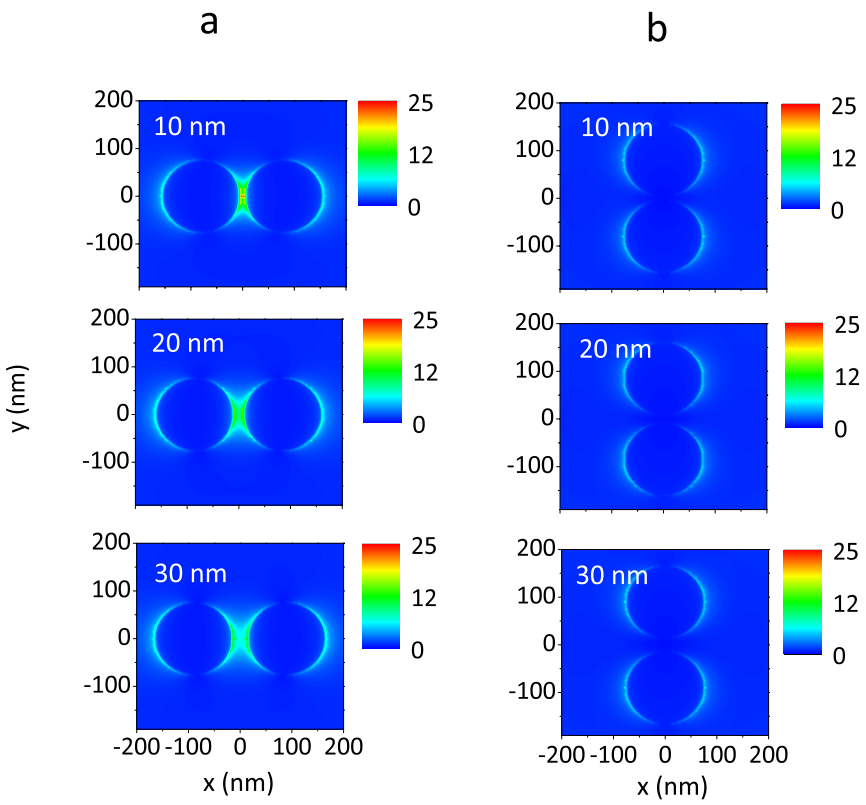

Figure 2.4. Near-field plots of longitudinal (a) and transverse (b) plasmon modes in Ni nanodimer particles with separations 10 nm, 20 nm and 30 nm, respectively, analytically

calculated for the wavelength 800 nm, employed in Paper 2. Image courtesy of Nicolò Maccaferri.

When individual plasmon modes interact, a low-energy (red-shifted) hybrid mode is obtained for in-phase oscillations with the incoming electric field of the charges of elementary nanoparticles whereas the out-of-phase oscillations represent the higher-energy mode that is blue-shifted. These in-phase and out-of-phase plasmon modes are also known as bonding and anti-bonding modes [27].

Multiple plasmon resonances occur for asymmetric particles such as pairs of metal nanoparticles, e.g. dimers, for different directions of light polarization. Depending on the direction of light polarization, *longitudinal* and *transverse* plasmon modes can be excited in a dimer particle (Fig. 2.4 and Fig. 2.5). For longitudinal light polarization the low-energy mode, or bonding mode, and the higher-energy mode, or antibonding mode, are accessible optically. At the same time, the anti-bonding mode for transversal light polarization is dark and can not be optically excited for a pair of identical nanodisks.

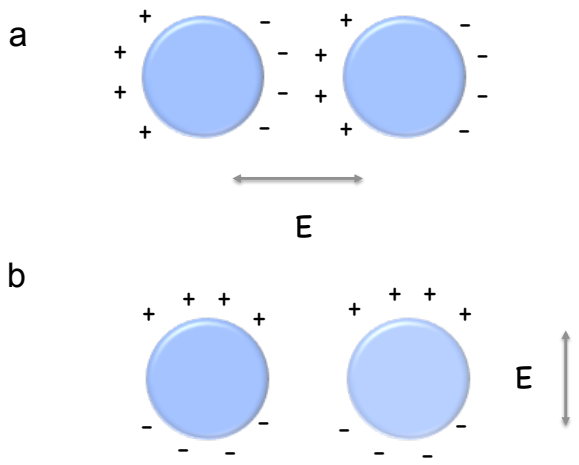

Figure 2.5. Illustration of electric dipole and plasma oscillations excited by localized plasmon resonance in a nanoparticle dimer for (a) bonding longitudinal and (b) optically accessible bonding transverse mode (following the definition given in [26]).

The restoring force, acting on the oscillating electrons is decreased due to Coulomb attraction between the opposite charges of neighboring particles for longitudinal light polarization when the bonding mode is excited (Fig. 2.5a), and increased due to Coulomb repulsion for transverse light polarization (Fig. 2.5b). Since the overall energy of the

configuration is decreased, there is a red-shift of the plasmon resonance for the excitation of longitudinal mode. Oppositely, the increase in energy results in a blue-shift of the transverse mode [1, 22, 28]. Consequently, the longitudinal resonance redshifts as the interparticle distance get smaller (Fig. 2.6a) whereas the transverse resonance is much less sensitive to distance change between the particles (Fig. 2.6b).

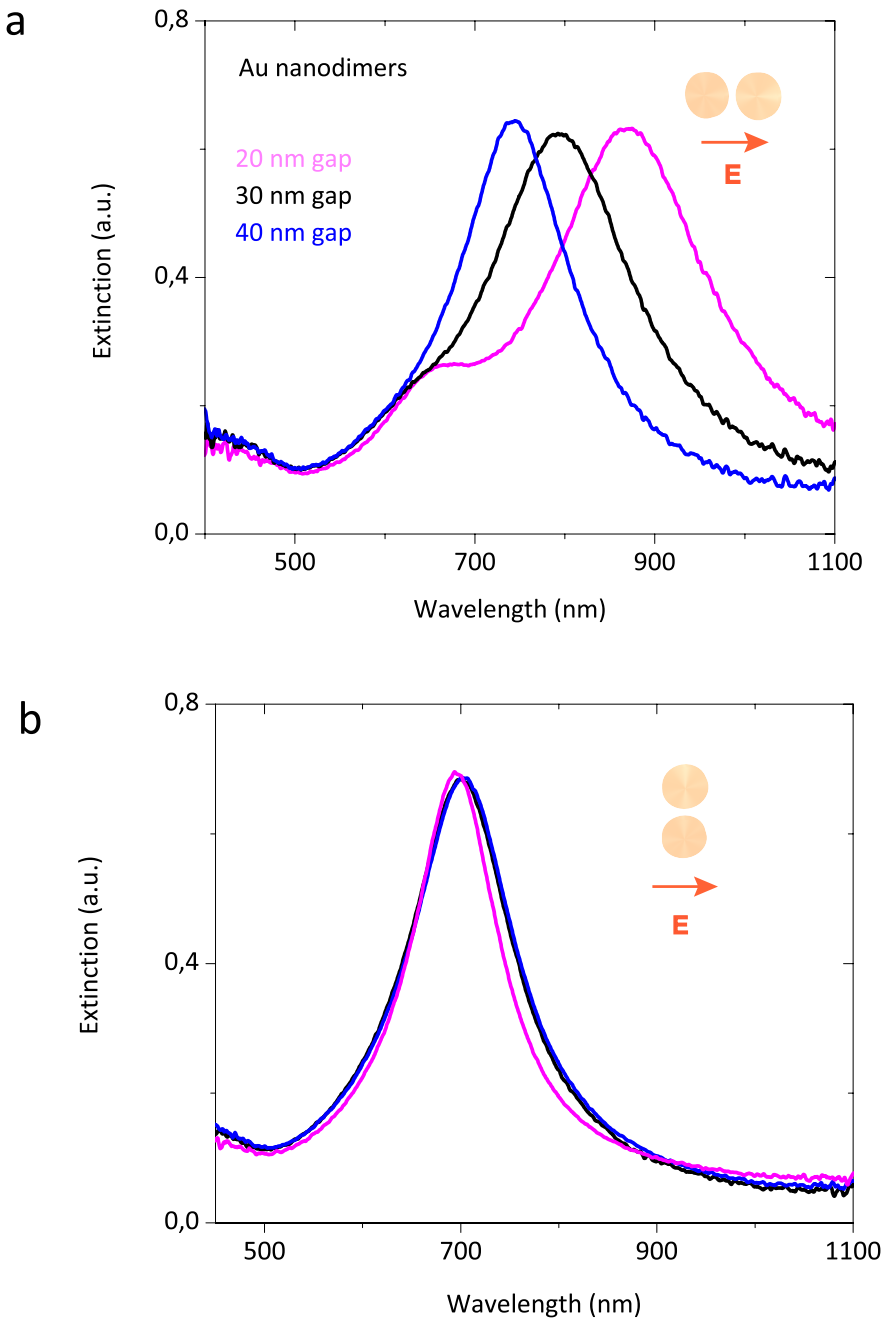

Figure 2.6. Longitudinal (a) and transverse (b) modes of localized plasmon resonances excited in Au nanodimers with interparticle separations 20 nm, 30 nm and 40 nm. The single disk diameter is 150 nm and the thickness is 30 nm.

2.3 Plasmon rulers

Accurate measurements of distances on the nanoscale are decisive in many aspects of the materials and life sciences. Prominent examples include studies of various biochemical processes via conformational changes in biomolecules. Previously, the optical tools used to obtain spatial information on the nanoscale, and down to the single-molecule level, focused on Förster resonance energy transfer (FRET) spectroscopy and the use of organic fluorophores in so-called molecular rulers. Dynamic processes, such as DNA bending and cleavage, and RNA catalysis and folding, as well as protein–protein interactions, were all first explored by FRET. However, the limitation of fluorophores due to their photo bleaching and degradation over time led to the emergence of noble-metal nanoparticle-based plasmon rulers [29-32]. The operation of plasmon rulers relies on localized collective electronic oscillations (localized plasmons) in nanometal assemblies and on the near-field coupling (i.e., hybridization) between the plasmon modes of the adjacent nanoparticles, which strongly depends on the interparticle distance [26, 33]. Plasmon local electromagnetic near-fields exponentially decay over distance and as such, at small separations, the near-field enhancement and coupling effects increase dramatically. The underlying idea of a plasmon ruler, which consists of two or more noble metals or elements of core–shell structures, is then the extreme sensitivity of the light scattering to the interparticle gap size [26, 27, 33-38]. This was first explored with nanoplasmonic dimer antennas almost a decade ago for monitoring the kinetics of single DNA hybridization events in solution (Fig. 2.7 that also explains the working principle of a plasmon ruler) [29].

In later realizations, plasmon rulers with sub-nm resolution consisted of thin-film coupled single-particle nanoantennas that utilized thiol monolayers with an adjustable chain length [30]. The principles of plasmon ruler design are typically refined with lithographically fabricated nanoantennas that are implemented to investigate the distance dependence of plasmon-coupling effects and to derive a plasmon ruler equation [31]. This includes the concept of a multielement three-dimensional plasmon ruler [32] to track the complex conformational changes that have also been recently realized in solution [39].

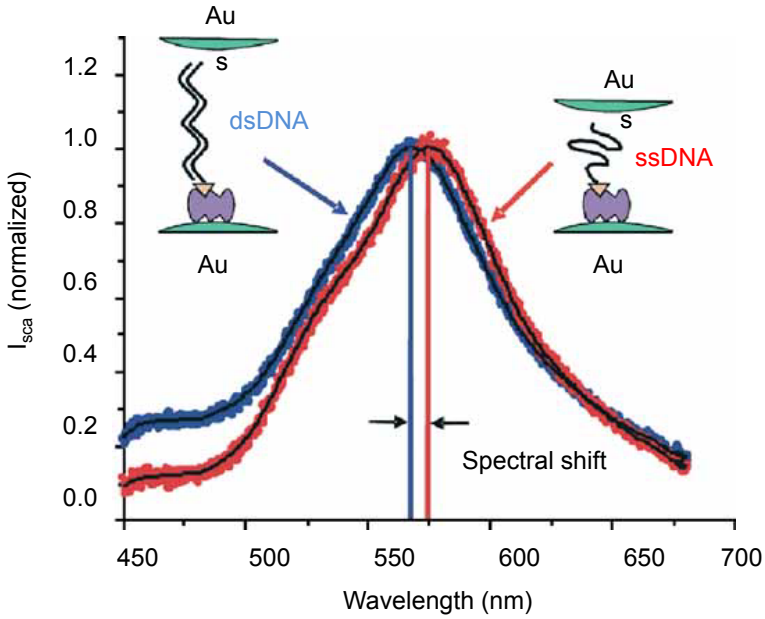

Figure 2.7. Spectral shift between a gold particle pair connected with ssDNA (red) and dsDNA (blue) also explaining the working principle of a plasmon ruler. The figure is taken from the reference [39].

In Paper 2 we introduce a conceptually new active plasmon ruler that employs magnetoplasmonic coupling instead of purely plasmonic coupling and allows optical detection of nanoscale distances. The ruler optimizes its own spatial orientation due to active operation and provides a figure-of-merit substantially exceeding the traditional plasmon rulers based on noble metals.

"Thus is established, I think for the first time, a true, direct relation and dependence between light and the magnetic and electric forces; and thus a great addition made to the facts and considerations which tend to prove that all natural forces are tied together, and have one common origin. It is, no doubt, difficult in the present state of our knowledge to express our expectation in exact terms; and, though I have said that another of the powers of nature is, in these experiments, directly related to the rest, I ought, perhaps, rather to say that another form of the great power is distinctly and directly related to the other forms; or, that the great power manifested by particular phenomena in particular forms, is here further identified and recognized, by the direct relation of its form of light to its forms of electricity and magnetism."

Michael Faraday on observation of the polarization rotation in polarized ray sent through a magnetized optical glass, 1845

3 Magnetoplasmonics with optical nanoantennas

Chapter 3 is focusing on magneto-optics and magnetoplasmonics with optical nanoantennas. In section 3.1 I give a short introduction to magneto-optics and classification of different magneto-optical phenomena. Thereafter, I focus on the magneto-optical Kerr effect and provide the analytical description of optical properties of gyrotropic medium. In section 3.2 I describe the role of localized plasmons and spin-orbit coupling on magneto-optical activity, and derive the analytical expressions for the Kerr ellipticity and Kerr rotation. I close this chapter by explaining the fundamental property of localized plasmons to enhance and tailor the magneto-optical activity.

3.1 Magneto-optical effects

Magneto-optical effects appear when light interacts with matter subjected to a magnetic field. The origin of these effects is system energy splitting, known as Zeeman effect, which occurs in external magnetic field. The presence of a magnetic field is not necessary if a matter is magnetically ordered (ferromagnetic, ferrimagnetic, etc.), so magneto-optic effects appear in the absence of external magnetic field as well. In a magnetized matter, the magnetic field breaks the spatial and time-reversal symmetries leading to optical anisotropy, which manifests itself as dichroism, i.e. difference in the absorption coefficients for two orthogonal polarizations. Dichroism is defined as the difference between absorptions of the right-hand and left-hand circularly polarized components ($k_+ - k_-$) in the Faraday geometry (when $k \parallel H$), so-called *magnetic circular dichroism* (MCD). In Voigt geometry, when $k \perp H$, it is known as *magnetic linear dichroism* (MLD), or the difference between absorptions of components polarized parallel and perpendicular to the magnetic field. The splitting in dispersion curves of the absorption coefficient is related to the splitting in dispersion curves of the refractive index via Kramers-Kroning relations. It is observed as the difference between the refractive indices for the two circularly polarized components (also known as *magnetic circular birefringence* or *Faraday effect*) and for the two linearly polarized components (*magnetic linear birefringence*) in the Faraday and Voigt geometry, respectively [40].

The origin of dichroism and birefringence lies in symmetry breaking induced by a magnetic field. Magnetic field is an axial vector and has symmetry of circular current set out in a plane perpendicular to the vector of the magnetic field. Therefore, if a medium is placed in a magnetic field, the rotation directions in the plane perpendicular to the magnetic field are different. This means that in a magnetized medium the optical properties of light propagating along the magnetic field direction with right-hand and left-hand circular polarizations are different too. The interesting analogy is symmetry breaking in a rotating medium along its rotational axis, which is explained by the fact that angular velocity, like magnetic field, is an axial vector [21, 40].

3.1.1 The Faraday effect

In 1845 Michael Faraday discovered that if a block of optical quality (heavy) glass, borosilicate of lead, is placed in a magnetic field, it becomes optically active [41]. When linearly polarized light passes through glass in a direction parallel to the applied magnetic field, the polarization plane is rotated by an angle Θ, which is proportional to the magnitude of the magnetic field H and the distance L, travelled by light:

$$\Theta = VHL. \tag{1}$$

The proportionality constant V, called the Verdet constant, is defined as the rotation per unit path, per unit field strength and depends on the material properties, photon energy and the temperature.

The Faraday effect originates from the difference in refractive indices of right-hand and left-hand circularly polarized components, $n_+ - n_-$, induced by the magnetic field. Linearly polarized light can be seen as a superposition of left- and right-hand circular waves with a defined phase difference. As a result of the difference between n_+ and n_-, the circular waves will propagate with different velocities c/n_+ and c/n_- when a magnetic field is applied, which causes the rotation of the polarization plane of the linearly polarized light by the angle [40]

$$\Theta = \frac{\omega}{2c}(n_+ - n_-)L, \tag{2}$$

where ω is angular frequency, c is the velocity of light and L is the path of the beam in the medium. The phenomenological distinction of Faraday effect from natural optical activity (chirality) is non-reciprocity of the Faraday effect: the value of Θ will be doubled if light travels back along the same path through the magnetized medium (e.g. after reflection from a mirror). In case of natural optical activity, when light travels back after normal reflection, $\Theta = 0$.

3.1.2 Magneto-optical Kerr effect (MOKE)

Along with magneto-optical effects arising during transmission of light through a magnetized medium, there are a number of effects, which manifest themselves when the light is reflected from a surface of a magnetized material. These phenomena are conventionally referred to as magneto-optical Kerr effects, discovered in 1877 by a Scottish physicist John Kerr, and can be classified to *longitudinal (meridional)*, *polar* and *transverse* (*equatorial*) Kerr effects according to the orientation of the magnetization vector relative to the reflective surface, or the plane of incidence of the incoming beam. Faraday and Kerr effects are *odd* effects, i.e. change sign when the sample is remagnetized [40].

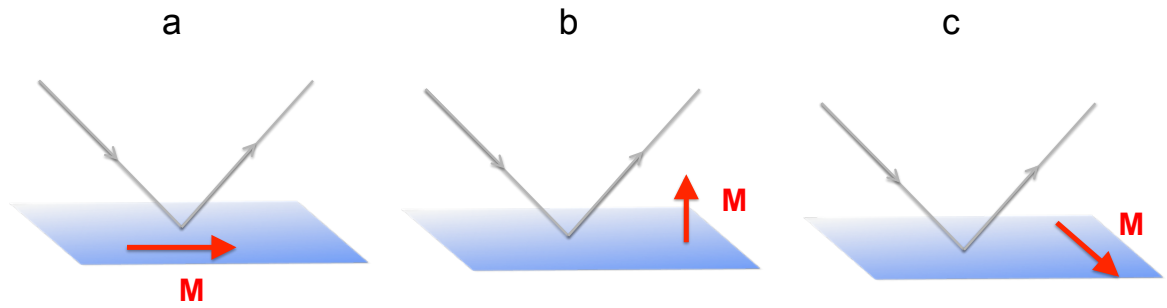

Figure 3.1. Geometry of the magneto-optical Kerr effect, showing the orientation of the vector of magnetization M with respect to the plane of light incidence in three configurations: (a) longitudinal, (b) polar and (c) transverse.

L-MOKE: In the longitudinal magneto-optical Kerr effect (L-MOKE) (Fig. 3.1a), the magnetization vector M lies both in the plane of the sample and in the plane of light incidence. In this effect, the polarization plane of the linearly polarized light is rotated and an ellipticity is introduced after the reflection from a magnetized surface (Fig. 3.2a).

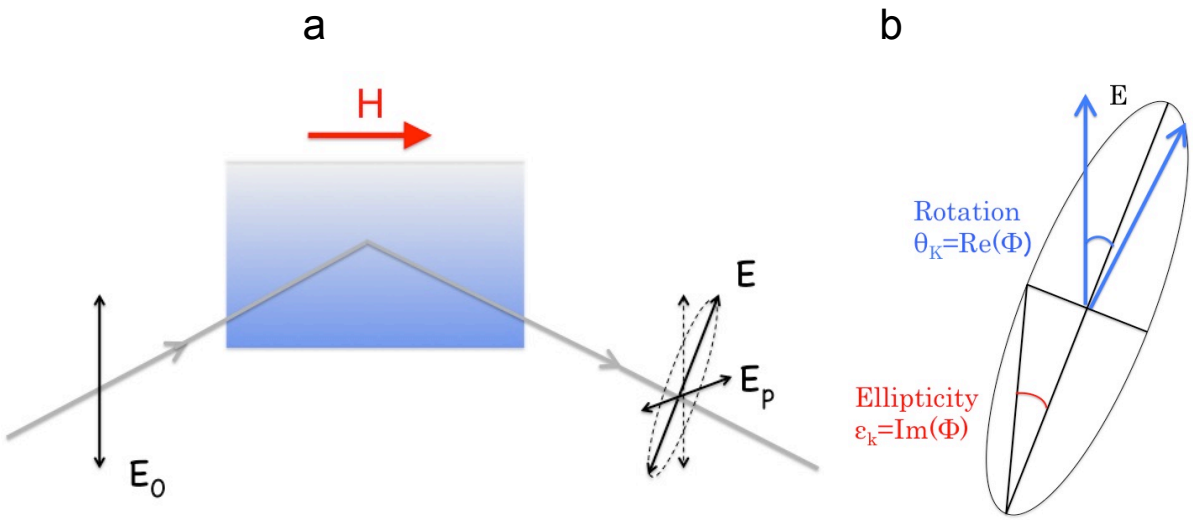

Figure 3.2. (a) Illustration of the rotation of the polarization plane and appearance of the elliptical component in L-MOKE. (b) Geometrical representation of the complex Kerr angle.

Kerr rotation and Kerr ellipticity compose the complex Kerr angle Φ_K (Fig. 3.2b) with Kerr rotation being its real part, $\Re[\Phi_K]$, and Kerr ellipticity being its imaginary part, $\Im[\Phi_K]$:

$$\Phi_K = \theta_K + i\epsilon_K. \tag{1}$$

Similar to the Faraday effect, L-MOKE is proportional to the magnetization and is primarily used to probe the magnetization of the sample being one of the most sensitive and simplest methods (Fig. 3.3). It is the main experimental technique used in this thesis to explore the magneto-plasmonic properties.

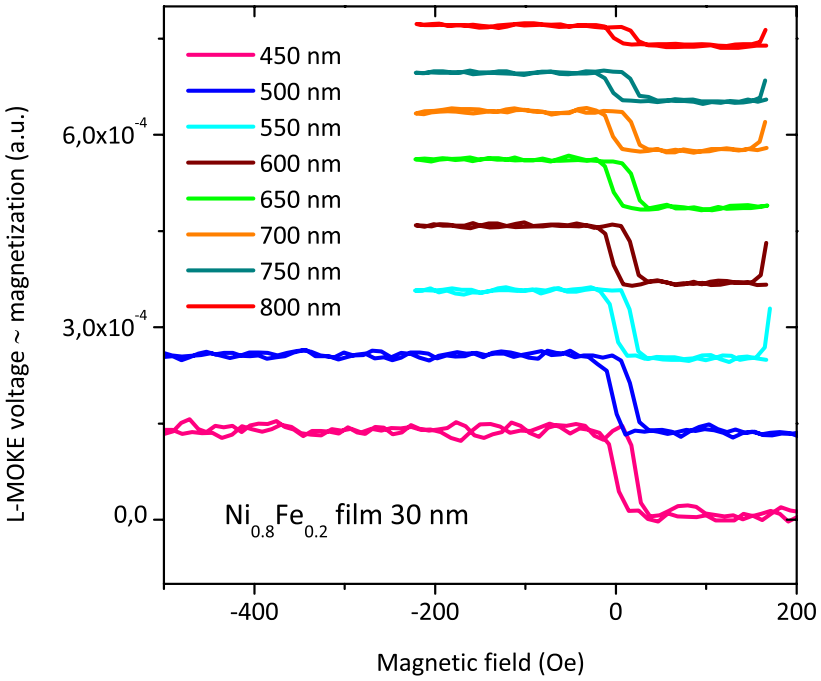

Figure 3.3. Magnetization hysteresis loops measured in permalloy ($Ni_{0.8}Fe_{0.2}$) film of the thickness 30 nm at wavelengths 450 nm, 500 nm, 550 nm, 600 nm, 650 nm, 700 nm, 750 nm and 800 nm by L-MOKE. The loops (apart from the one measured at 450 nm) are shifted from zero vertically for clarity of presentation and have the same scale.

P-MOKE: In the polar magneto-optical Kerr effect (P-MOKE), the magnetization vector *M* is oriented perpendicularly to the reflective surface and parallel to the plane of light incidence (Fig. 3.1b). Similarly to L-MOKE, this effect results in a rotation of the polarization plane and the appearance of ellipticity, though, giving values about one order of magnitude higher than L-MOKE. A common feature of the longitudinal and the polar MOKE is a presence of non-zero projection of the wave vector *k* on the magnetization plane. Polar Kerr effect is of great importance for optical data storage since it is used for reading the information from magneto-optical disks [40].

T-MOKE: In the transverse Kerr effect (T-MOKE), the magnetization vector is oriented perpendicularly to the plane of light incidence (Fig. 3.1c). It can only be observed for absorbing materials and results in intensity variation and phase shift of linearly polarized light reflected from a magnetized material. This effect is employed in observations of magnetic domains at the surface of a magnetized sample and in design of non-reciprocal

optical devices, such as transversely magnetized mirrors [40].

3.1.3 Dielectric tensor of gyrotropic medium

The dielectric permittivity tensor of an isotropic material is given by:

$$\varepsilon = \begin{pmatrix} \varepsilon_{xx} & 0 & 0 \\ 0 & \varepsilon_{yy} & 0 \\ 0 & 0 & \varepsilon_{zz} \end{pmatrix}, \quad (1)$$

where the diagonal elements $\varepsilon_{xx} = \varepsilon_{yy} = \varepsilon_{zz} = \varepsilon$ and non-diagonal elements $\varepsilon_{ij} = 0, i \neq j$. In the medium which exhibits magneto-optical (MO) effects (gyrotropic medium), the dielectric tensor becomes non-diagonal [42]:

$$\varepsilon = \begin{pmatrix} \varepsilon_{xx} & \varepsilon_{xy} & \varepsilon_{xz} \\ \varepsilon_{yx} & \varepsilon_{yy} & \varepsilon_{yz} \\ \varepsilon_{zx} & \varepsilon_{zy} & \varepsilon_{zz} \end{pmatrix} = \begin{pmatrix} \varepsilon & -iQm_z & iQm_y \\ iQm_z & \varepsilon & -iQm_x \\ -iQm_y & iQm_x & \varepsilon \end{pmatrix}. \quad (2)$$

Here Q is the magneto-optical Voigt parameter and m_i is the magnetization in i-direction. The appearance of non-diagonal terms in the dielectric tensor is defined by the direction, in which the magnetic field is applied. If z is the direction of light propagation, xy is the sample plane, and the magnetic field or magnetization is aligned in z-direction (the case of P-MOKE), the dielectric tensor takes form:

$$\varepsilon_{P-MOKE} = \begin{pmatrix} \varepsilon & -iQm_z & 0 \\ iQm_z & \varepsilon & 0 \\ 0 & 0 & \varepsilon \end{pmatrix}. \quad (3)$$

Similarly, when the magnetic field is applied in x-direction (L-MOKE) and in y-direction (T-MOKE), the tensor is given by (4) and (5):

$$\varepsilon_{L-MOKE} = \begin{pmatrix} \varepsilon & 0 & 0 \\ 0 & \varepsilon & -iQm_x \\ 0 & iQm_x & \varepsilon \end{pmatrix}, \quad (4)$$

$$\varepsilon_{T-MOKE} = \begin{pmatrix} \varepsilon & 0 & iQm_y \\ 0 & \varepsilon & 0 \\ -iQm_y & 0 & \varepsilon \end{pmatrix}. \quad (5)$$

The presence of non-diagonal elements in the dielectric tensor means that the respective components of the electromagnetic field become coupled by the spin-orbit (SO) interaction. MO is a result of SO interaction that couples transverse magnetic (TM or p) and transverse electric (TE or s) in a material and induces the change in the polarization state of the light. Specifically, when s-polarized (p-polarized) light reflects from the magnetized surface, it acquires a small p-polarized (s-polarized) component (Fig. 2a). The change in polarization state is described by non-diagonal Fresnel coefficients r_{ps} and r_{sp}, accounting for the polarization conversion, while the diagonal elements r_{pp} and r_{ss} are the reflection coefficients for p-polarized and s-polarized electromagnetic waves. One can express the complex Kerr angle, Kerr rotation θ_K and Kerr ellipticity ϵ_K, as follows:

$$\Phi_k = \theta_K + i\epsilon_K = \frac{r_{ps}}{r_{pp}}, \tag{6}$$

$$\theta_K = \Re\left(\frac{r_{ps}}{r_{pp}}\right), \tag{7}$$

$$\epsilon_K = \Im\left(\frac{r_{ps}}{r_{pp}}\right). \tag{8}$$

The non-diagonal Fresnel coefficients r_{ps} are responsible for polarization conversion and represent pure magneto-optical contribution to magneto-optical activity of the system, whereas the diagonal elements r_{pp} represent pure optical contribution to MO. Therefore, the overall MO response of the system may be enhanced by either increasing the MO contribution or reducing the optical contribution. An important property of localized surface plasmon resonance, namely strongly enhanced local fields, gives the enhancement in MO activity [43].

3.2 Effects of plasmons on magneto-optical activity

Localized plasmon resonances, due to the local field confinement at the nanoscale, result in greatly enhanced EM near-fields. Strongly enhanced local electric fields results in the enhanced interaction with magnetic fields, leading to the enhancement of the MO activity. Despite the decreased amount of the active material, which is the consequence of

nanopatterning, the Kerr rotation values become greatly enhanced due to the excitation of localized surface plasmons, and may, like in Ni, at some wavelengths exceed the values measured for continuous films of the same thickness (Fig. 3.4).

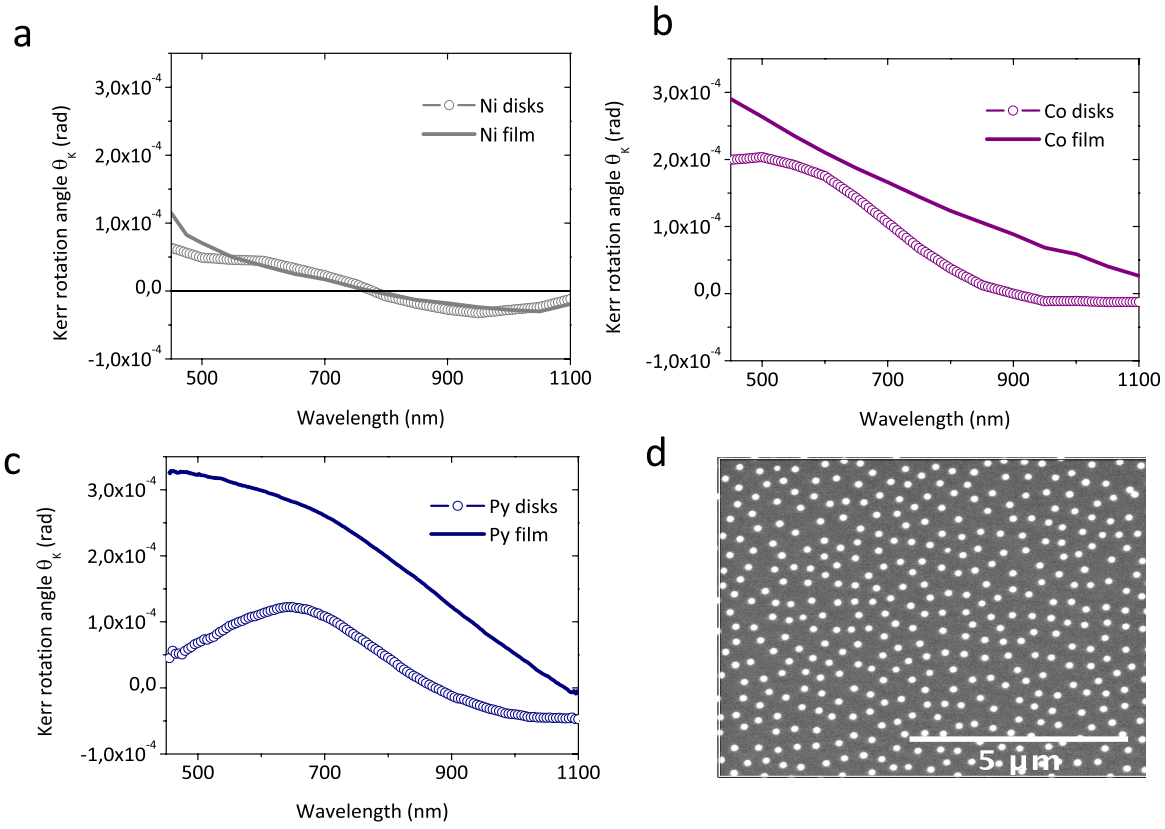

Figure 3.4. Kerr rotation measured by L-MOKE in continuous films and nanodisks of the same thickness made of (a) Ni; (b) Co; (c) Permalloy ($Ni_{0.8}Fe_{0.2}$). (d) Scanning electron micrograph of permalloy nanodisks with diameter 170 nm and thickness 30 nm.

In addition to strong enhancement of the magneto-optical activity by plasmons, a broadband tunability can be achieved in magnetoplasmonic nanostructures. Localized plasmon resonances can be supported by purely ferromagnetic nanostructures; however, they exhibit a much stronger damping due to a large imaginary part of the dielectric constant [44]. It has been recently demonstrated that plasmon excitations in ferromagnetic nanoparticles induce the sign reversal of Kerr rotation and ellipticity [14], and allow the tuning of MO activity [13, 14], which, being an intrinsic property of matter, in principle, can not be freely manipulated. In noble metals the MO response is much weaker than in ferromagnetic materials and has to be accessed with very strong magnetic fields of several Tesla, compared to (0.5-1) Tesla in ferromagnetic materials. However, due to the huge near-fields induced by plasmon resonance excitation in noble metals, they can exhibit a sizable

MO activity at low magnetic fields (of the order of 1 Tesla) [45, 46]. Unfortunately, localized plasmon resonances in ferromagnetic materials are strongly damped and broadened due to high absorption and do not produce as high local fields as in noble metals (Fig. 3.5). A promising route in magnetoplasmonics is a design of hybrid nanostructures, combining a ferromagnetic and a noble material [12, 47], where the MO response can be boosted due to strong electromagnetic field enhancement. Moreover, by proper stacking the magnetic and plasmonic components it is possible to generate the MO activity in a non-magnetic element, with overall MO response exceeding the MO response of pure magnetic system [48-50] and significantly reduced optical losses [47].

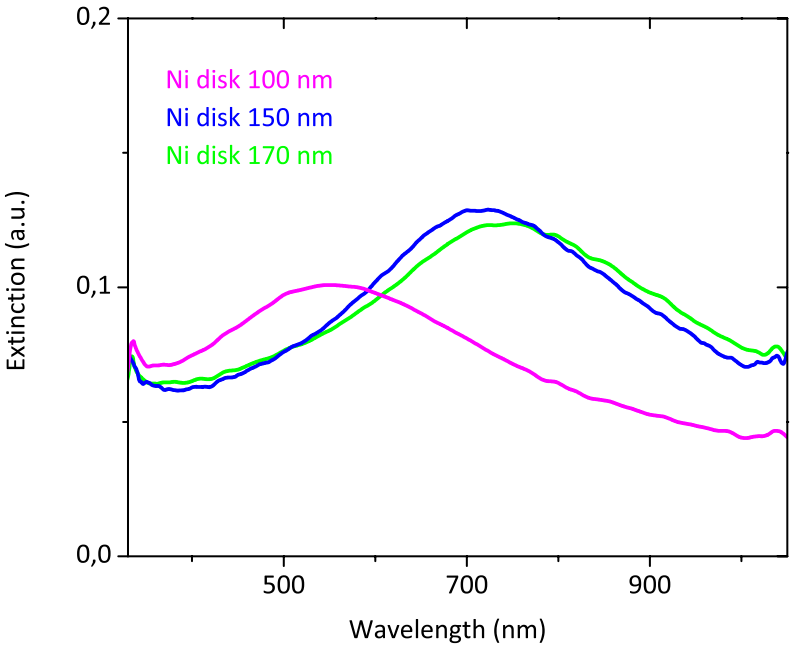

Figure 3.5. Localized plasmon resonances in Ni nanodisks with diameters 100 nm, 150 nm and 170 nm and thickness 30 nm.

3.2.1 Spin-orbit coupling effects on the magneto-optical activity

The interaction between plasmon resonances and MO activity can be understood from the derivation of polarizabilities of a single nanodisk, located in a magnetic field [51]. In L-MOKE geometry (Fig. 3.6a), the incident electric field E^0 along the y-axis induces an electric dipole along this axis, given by:

$$p_y = \alpha_{yy} E_y^o. \quad (1)$$

The electron oscillations along the y-axis are coupled via the spin-orbit (SO) interaction with the magnetization M, which is oriented along the x-axis. This coupling results in a dipole oscillation in the transverse direction along the z-axis. The expression for this dipole can be written in terms of non-diagonal elements of the polarizability tensor, as [51]:

$$p_z = \alpha_{zy} E_y^o. \tag{2}$$

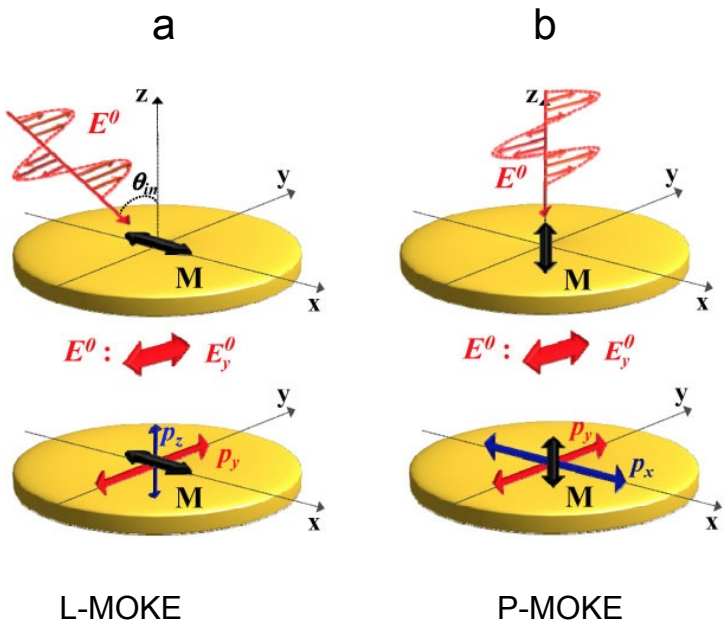

Figure 3.6. Longitudinal (a) and polar (b) MOKE configurations for an isolated nanodisk with xz being the scattering plane. In L-MOKE (left), the incident electric field E_y^o induces a direct dipole p_y, which generates a dipole p_z through the spin-orbit coupling. In P-MOKE (right), the incident electric field E_y^o is exciting p_y and spin –orbit induced dipole p_z. The figure is adapted from [51].

As it is explicitly shown in [51], the general expression for the non-diagonal elements of the polarizability tensor is given by:

$$\alpha_{kj} = \frac{\varepsilon_{kj}\alpha_{kk}\alpha_{jj}}{(\varepsilon - \varepsilon_m)^2}, \tag{3}$$

with ε_m being the dielectric permittivity of the surrounding medium and ε_{kj}, the non-diagonal elements of the dielectric tensor

$$\varepsilon = \begin{pmatrix} \varepsilon_{xx} & \varepsilon_{xy} & \varepsilon_{xz} \\ \varepsilon_{yx} & \varepsilon_{yy} & \varepsilon_{yz} \\ \varepsilon_{zx} & \varepsilon_{zy} & \varepsilon_{zz} \end{pmatrix}. \tag{4}$$

The diagonal elements of polarizability tensor α_{ii} of a single nanodisks are defined by the expression [52]:

$$\alpha_{ii} = \frac{\varepsilon_m(\varepsilon - \varepsilon_m)}{\varepsilon_m + N_{ii}(\varepsilon - \varepsilon_m)}, \tag{5}$$

were N_{ii} is depolarizing factor along i-direction.
By setting $k = z$ and $j = y$ in formula (2), the expression for the electric dipole, induced by SO coupling is obtained as follows:

$$p_z = \alpha_{zy} E_y^o = \left[\frac{\varepsilon_{zy}\alpha_{yy}\alpha_{zz}}{(\varepsilon - \varepsilon_m)^2}\right] E_y^o. \tag{6}$$

In P-MOKE geometry illustrated in Fig. 3.6b, the electric field E_y^o at normal incidence induces an electric dipole $p_y = \alpha_{yy} E_y^o$, which now is coupled through SO coupling with magnetization M in x-direction. This coupling results in a transverse dipole along x-axis, according to (3):

$$p_x = \alpha_{xy} E_y^o = \left[\frac{\varepsilon_{xy}\alpha_{xx}\alpha_{yy}}{(\varepsilon - \varepsilon_m)^2}\right] E_y^o. \tag{7}$$

The MO activity is completely determined by the transverse localized plasmon resonances induced by the spin-orbit coupling and is not influenced by the plasmon resonances excited by direct illumination. This will be discussed in the next section.

3.2.2 Tailoring the magneto-optical activity with plasmons

In analogy with formula (6) in 3.1.3 and using the expressions for p_y and p_z in 3.2.2, the complex Kerr angle in L-MOKE configuration (as it is presented in Fig. 3.6a in previous section 3.2.1) can be extracted:

$$\Phi_k{}^L = \frac{p_z}{p_y} = \frac{\varepsilon_{zy}\alpha_{yy}\alpha_{zz}\sin\theta_{inc}}{(\varepsilon-\varepsilon_m)^2\alpha_{yy}}, \tag{1}$$

where $\sin\theta_{inc}$ accounts for the angular dependence of spin-orbit induced dipole p_z, when θ_{inc} is the incidence angle of the incoming electric field. Similarly, the expression for the complex Kerr angle in P-MOKE configuration is presented by:

$$\Phi_k{}^P = \frac{p_x}{p_y} = \frac{\varepsilon_{xy}\alpha_{yy}\alpha_{xx}}{(\varepsilon-\varepsilon_m)^2\alpha_{yy}}. \tag{2}$$

As we can notice, the terms α_{yy} related to the polarizabilities of directly excited dipole in the expression (1) and (2) cancel out. The fundamental consequence of these equations is that plasmon-induced enhancement and phase tuning of MO response occur due to the transverse resonance excited due to the SO coupling. From these expressions it follows that the non-diagonal terms in permittivity tensor are the key elements in broadband tunability of both Kerr rotation and Kerr ellipticity, composing the complex Kerr angle. This fundamental property motivates the engineering of complex 2D and 3D nanostructures where several spectrally separated plasmon resonances allow the broadband control of MO activity and the polarizabilities can be tailored at will [53]. As it is explicitly demonstrated in [13] and [53], controlling the shape and the size of magnetoplasmonic nanostructures opens up a possibility to tailor the polarization state of the reflected light and obtain hugely enhanced values of the Kerr rotation. Paper 1 explores the tunability of Kerr MO effect in 3D magnetoplasmonic antennas for all three MOKE configurations, namely L-MOKE, P-MOKE and T-MOKE.

4 Enter chiral plasmonics

4.1 Chirality and chiroptical effects

The life is fundamentally asymmetric and chirality can be found in all its forms, from proteins and DNA to macroscopic chirality in animal and plant kingdoms. In biology and organic chemistry, the two forms of a chiral molecule with different handedness are called right-handed and left-handed *enantiomers* with common notations *D* (*dextro*)- *and L* (*levo*)-*enantiomers* (coming from Latin *dexter,* 'right', and *laevus,* 'left') used in chemistry, or *R* - *and S- enantiomers* (from Latin *rectus* meaning 'straight' or 'clockwise' and *sinister* meaning 'left' or 'counterclockwise') used in biology. In fact many biomolecules display only one handedness and are stereo-selective, which means that chemical reactions with molecules of similar handedness are more favorable. Life is largely made of molecules that have only one handedness – most of amino acids, the building blocks of proteins, including 9 essential amino acids, are L-enantiomers, whereas carbohydrates, or sugars, are D-enantiomers.

The light is circularly polarized when the electric field vector $\vec{E}$ is rotating with constant amplitude. It is common to define *right circularly polarized light (RCP)* and *left circularly polarized light (LCP)* when the E field rotates clockwise or counter-clockwise, respectively, looking at the light coming from the source (see figure 4.1) [23]. Linearly polarized light can be represented as a superposition of RCP and LCP with equal amplitudes.

Figure 4.1. Illustrations of right circularly polarized light (RCP) (on the right) and left circularly polarized light (LCP) (on the left). The orange errors are showing the direction of light propagation, or the $\vec{k}$ vector of light, and the blue errors are showing a random orientation of the electric vector $\vec{E}$.

In general, the presence of chirality in the symmetry of a material will always lead to chiroptical effects– *circular birefringence (CB)* and *circular dichroism (CD)*. Circular birefringence, which is also referred to as natural *optical activity,* or *optical rotatory dispersion (ORD),* is a result of different propagation speeds, and thus refractive indices n, for left- and right circularly polarized light (Fig.4.2a). When linearly polarized light travels through a medium with circular birefringence, its left- and right circularly polarized components, LCP and RCP, will travel with different velocities, resulting in the rotation of light polarization plane. The CB, or ORD, is characterized by the rotation angle θ that can be expressed as follows:

$$\theta = \frac{\pi\,(n_{LCP} - n_{RCP})\,l}{\lambda}, \tag{1}$$

where n_{LCP} and n_{RCP} are the refractive indices for LCP and RCP, respectively, λ is the wavelength and l is the path length through the material.

Materials display *circular dichroism (CD)* when they absorb and/or scatter right- and left circularly polarized light differently due to different extinction coefficients k for left- and right circularly polarized light (Fig. 4.2b). When linearly polarized light propagates through a medium with circular dichroism, the amplitudes of its left- and right circularly polarized

components, LCP and RCP, will be altered and will no longer be equal (Fig. 4.2b) resulting in elliptical polarization state. This ellipticity is a direct measure of CD that can be expressed as follows:

$$CD\ (rad) = \tan\varepsilon = \frac{T_{RCP}^{1/2} - T_{LCP}^{1/2}}{T_{RCP}^{1/2} + T_{LCP}^{1/2}}, \tag{2}$$

where T_{RCP} and T_{LCP} are transmitted trough the medium intensities of RCP and LCP. Similarly to $n\ (\lambda)$ and $k\ (\lambda)$, $ORD\ (\lambda)$ and $CD\ (\lambda)$ spectra are Kramers-Kroning related and one can be mathematically derived from the other.

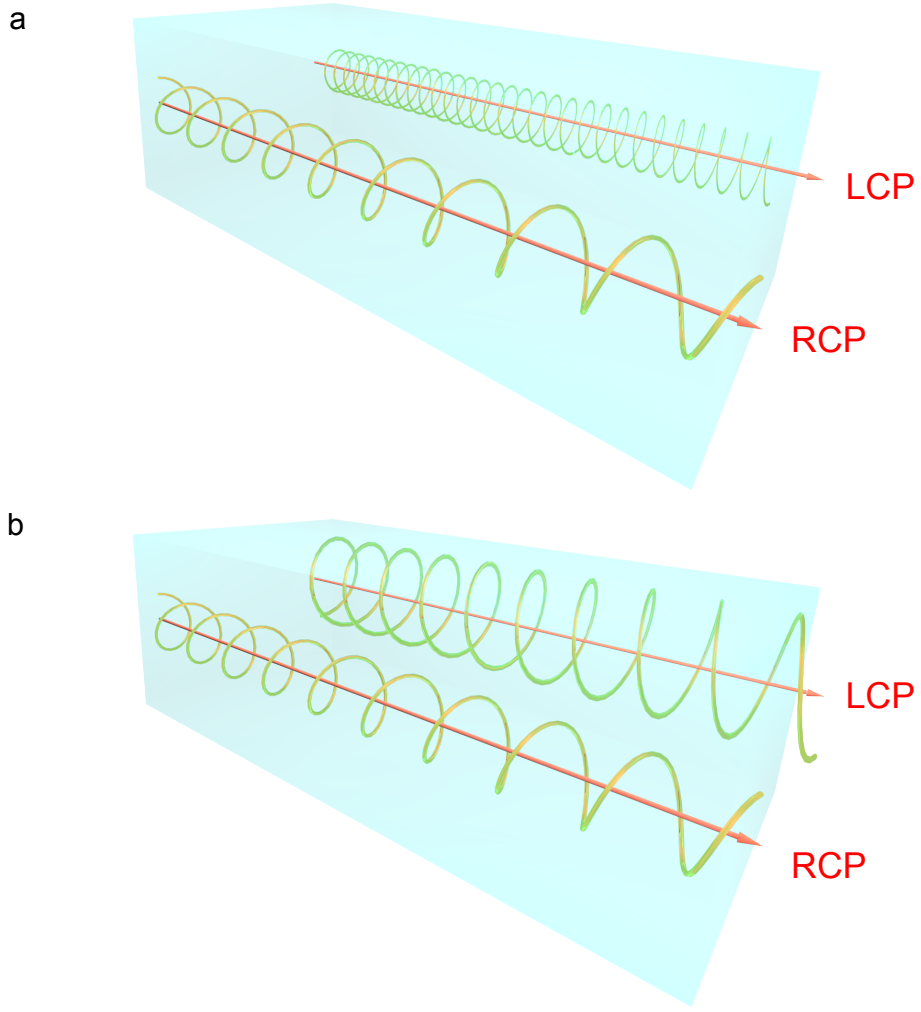

Figure 4.2. (a) Circular birefringence in a medium with different refractive indices n for RCP and LCP when $n_{LCP} < n_{RCP}$ and LCP propagates faster than RCP. (b) Circular dichroism in a medium with different extinction coefficients k for RCP and LCP when $k_{LCP} < k_{RCP}$ and LCP is less absorbed than RCP.

Naturally chiral materials like sugars, quartz and liquid crystals display optical activity and circular dichroism due to chiral symmetry of their molecules or, like liquid crystals, due to the arrangement of the achiral molecules in a helix. Chiroptical effects always emerge in the presence of chirality that can be categorized in two-dimensional (2D) planar chirality and tree-dimensional (3D) chirality. A 2D planar chiral object can't be superimposed on its mirror image by any *in-plane* rotation or translation, whereas a 3D chiral object preserves its handedness irrespective of the angle of observation, even if the object is rotated in 3D space. A helix (Figure 4.3a) and a spiral (Figure 4.3b) are the examples of 3D and 2D chiral objects.

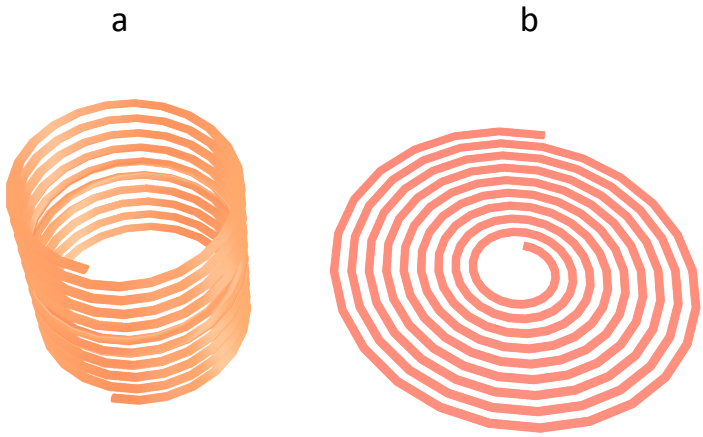

Figure 4.3. (a) 3D chiral object. (b) 2D planar chiral object.

The origin of chirality can be either intrinsic or extrinsic. The intrinsic chirality is created when the individual elements lack twofold rotational symmetry, or, when non-chiral elements are arranged in chiral geometry, like a double helix of DNA. The extrinsic chirality is formed when the mutual orientation of non-chiral elements and the wave propagation vector $\vec{k}$ lack mirror symmetry. For oblique light incidence case, the $\vec{k}$ vector breaks the time-reversal symmetry and its mutual arrangement with the normal to the surface lacks the symmetry, which leads to extrinsic chirality.

4.2 Chiral plasmonics: chirality on the nanoscale

In direct analogy with biochemical molecules, the term *circular dichroism* is widely used in plasmonics when one talks about plasmonic nanostructures that respond differently to

right- handed and left-handed circular polarized light. Artificial chiral materials have drawn an enormous attention in recent years where solid-state chiral materials based on plasmonic nanoantennas became potential candidates for new devices that can control light on the nanoscale. The reason why chiral plasmonic nanostructures became so attractive is that chiroptical effects become strongly enhanced due to the nanoconfinement of local electric fields and strong near-field coupling, which is of great benefit to chiral sensing [54]. Chiral plasmonic materials also provide a new route of controlling light on a sub-wavelength scale through the interaction with its helicity or the spin angular momentum [55]. Engineering of new chiral optical materials and surfaces that can manipulate the helicity of light would be decisive for the future optical spin-controlled nanophotonic devices that manipulate the transmission, absorption and scattering of light in helicity-dependent manner [56, 57].

In recent years many research groups focused on design and fabrication of chiral plasmonic geometries aiming at enhanced chiroptical effects [58]. The reports on plasmonic materials with 3D chiral geometry, such as plasmonic helix, demonstrate not only the presence of circular dichroism in chiral nanoantenna arrays [59] (Figure 4.4a), but also the possibility to obtain a huge CD signal of several degrees [60] (Figure 4.4b) and tailor the chiroptical response [60, 61] (Figure 4.4b, c).

It is worth to mention that the 3D optical nanoantennas geometry is not necessary for chiroptical response to emerge, and very recently Khanikaev et al. reported [62] that macroscopic CD does exist in 2D plasmonic systems due to Ohmic losses and can be detected in transmission experiment (Figure 4.5a). The work of Schnell et al. [63] shows the existence of optical chirality in 2D chiral Archimedean spiral nanoantennas by near-field mapping experiments (Figure 4.5b). Also recently it was shown that the chiral optical response can be generated in structurally symmetric nanoantennas due to materials asymmetry (i.e., using the combination of the materials with different optical properties – Au and Si in this particular case) instead [64] (Figure 4.5c). This fundamentally new concept of symmetric chiroptical materials is developed and employed in Papers 3 and 4 presented in this thesis.

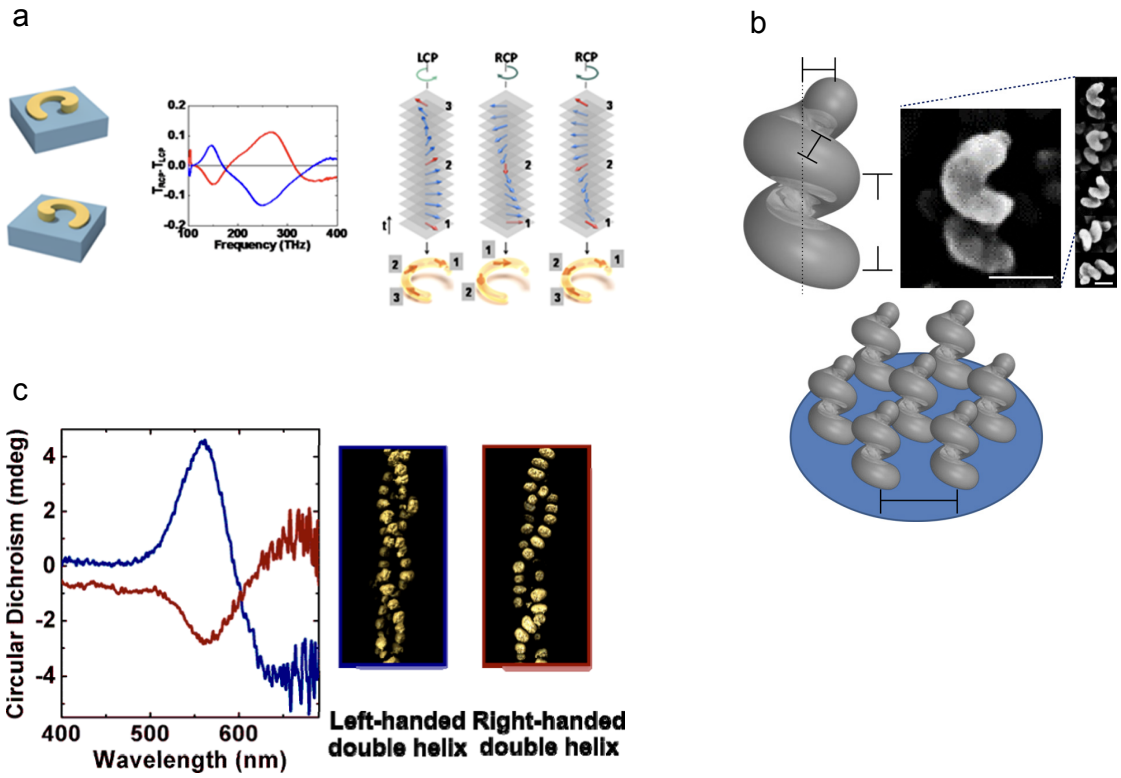

Figure 4.4. 3D chiral plasmonic materials. (a) 3D chiral plasmonic arrays from reference [59]. (b) Plasmonic nanohelices from reference [60]. (c) Helical nanoparticle superstructures from reference [61].

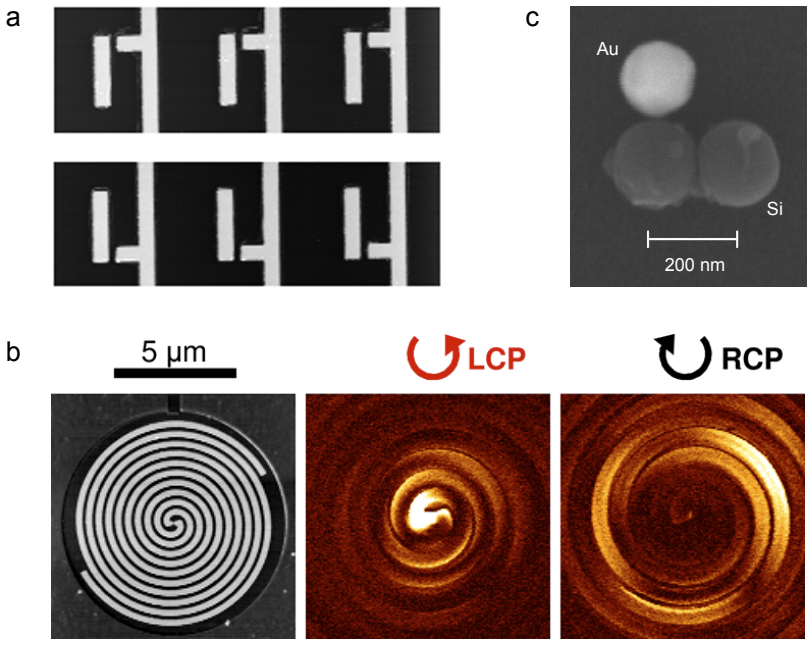

Figure 4.5. 2D chiral plasmonic materials. (a) Planar chiral plasmonic nanoantennas from reference [62]. (b) 2D chiral Archimedean spiral nanoantennas from reference [63]. (c) 2D chiral symmetric nanoantennas enabled by heteromaterial selection from reference [64].

Experimental methods

"But still try, for who knows what is possible? "

Michael Faraday

5 Nanofabrication

In this chapter, I will introduce nanofabrication methods that are fundamental in all works in this thesis and are based on hole-mask colloidal lithography (HCL). HCL is a technique that was developed at Chalmers University of technology in 2007 and since then many groups in the fields of nanoplasmonics, plasmonic sensing and bio-sensing have been employed it worldwide. In contrast to electron-beam lithography, which is rather expensive, time consuming and has a limited scale of ~ μm^2, one can produce nanostructures with cm^2-scale by affordable and highly parallel HCL method. HCL method is used to fabricate an evaporation mask and is always followed by physical vapor deposition (PVD), which is a thin film deposition technique and uses a high-energy electron beam to create a physical vapor that is evaporated onto the substrate.

5.1 Standard protocol for hole-mask colloidal lithography (HCL)

Hole–mask colloidal lithography (HCL) [65] is a bottom-up nanofabrication method utilizing the self-assembly of negatively charged sulfate latex microspheres also referred to as polystyrene (PS) beads.

1. We use microscope slide glass (VWR International) of dimensions 10 mm × 10 mm × 1 mm as a substrate. The substrate is cleaned by ultrasonication in acetone and exposed to reactive ion etching (RIE) by oxygen O_2 plasma (5 s, 50 W, 250 mTorr, Plasma Therm BatchTop PE/RIE m/95) in order to increase polymer adhesion to the glass (Figure 5.1a).

2. The layer of polymethyl methacrylate (950PMMA 4% diluted in anisole, MW = 950000, MicroChem), 235 nm thick, is spin-coated on the substrate and baked at 180 °C in a convection oven for 10 min (Figure 5.1b).

3. After baking, O_2 plasma is applied for 5 s to make the PMMA hydrophilic.

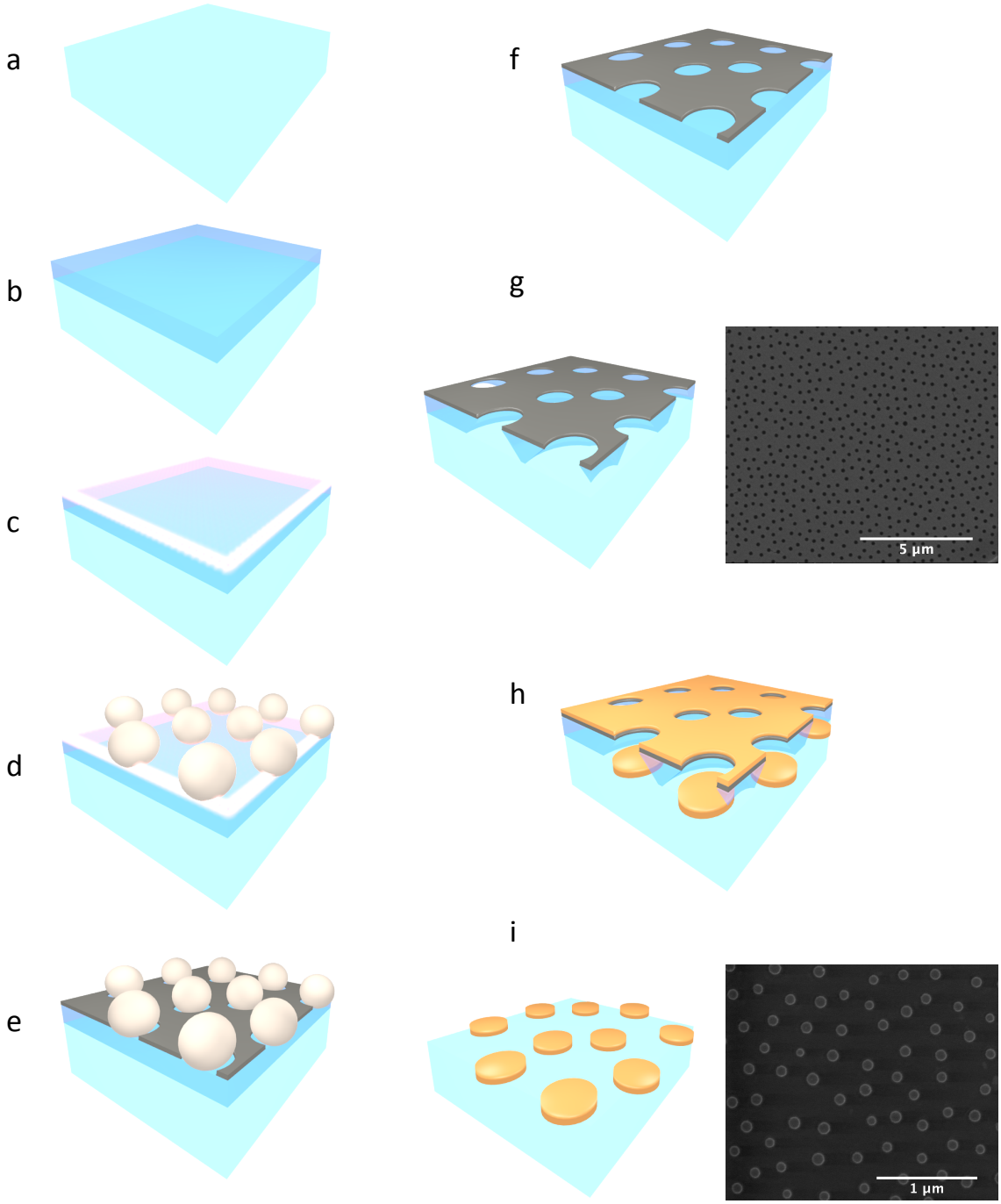

Figure 5.1. Hole-mask colloidal lithography step by step. (a) Glass substrate after cleaning and O_2 plasma treatment. (b) Spin-coating of PMMA. (c) Treatment of PMMA layer with PDDA. (d) Deposition of polystyrene beads. (e) Evaporation of the Cr mask. (f) Tape stripping of the polystyrene beads. (g) O_2 plasma etching (left panel) and SEM micrograph of the final hole-mask (right panel). (h) Evaporation of metallic layer through the hole-mask. (i) Lift-off in acetone (left panel) and SEM micrograph of single nanodisk antennas (right panel).

4. In the next step, the substrate with the PMMA layer residing on it is functionalized with polydiallyldimethylammonium chloride (PDDA, MW = 200000–350000, 0.2% solution in deionized (DI) water), and then rinsed with DI water and finally dried using nitrogen N_2 gun applied normally to the sample surface (Figure 5.1c).

5. Negatively charged polystyrene beads (sulfate latex beads, 0.2% suspended in DI water, Invitrogen) are pipetted onto the substrate and kept there for ~120 s. After careful rinsing with DI water, the substrate is immediately dried with the N_2 gun at normal flow incidence to avoid bead removal or aggregation (Figure 5.1d).

6. As a next step, a physical vapor deposition (PVD) is used for evaporation of a very thin Cr layer of 10nm (Figure 5.1e), which is then followed by tape stripping of the spheres (SWT-10 tape, Nitto Scandinavia AB) resulting in a hole-mask, which resides on the top of PMMA layer (Figure 5.1f).

7. Reactive ion etching (RIE) by O_2 plasma is applied to etch through the entire thickness of the PMAA layer resulting in final evaporation mask (Figure 5.1g).

8. The evaporation mask can be used to fabricate a variety of nanostructures [65] such as single nanodisks when a metallic layer of a desired thickness is deposited through the mask by PVD at very low pressure $\sim 5 \cdot 10^{-7}$ Torr (Figure 5.1h) and the process is finished by a lift-off in acetone (Figure 5.1i).

Next, I describe some important details that one needs to consider for producing homogeneous and aggregation-free samples with a nice particle distribution.

Note 1: It is very important to avoid the formation of air bubbles in the step 2 while pipetting PMMA onto the glass substrate. Therefore the substrate should be carefully cleaned in step 1 and the pipette should be brought very close with a small droplet of PMMA pipetted onto the glass. Small dust particles and air bubbles would make a spin-coated PMMA layer ununiform and would result in ununiform samples.

Note 2: The PS bead removal after rinsing in Step 5 is the most challenging in whole HCL process and, if not performed correctly, may result in formation of defects. The N_2 flow should be strong and should applied normally to the surface to remove most of the water. After that, there will still be some small amount of water left due to the capillary forces and one should be very careful while removing that with N_2 gun. This water is easily moved across the sample surface by the strong N_2 flow, which will destroy the electrostatic balance

between PS beads forming “tracks” and other defects. To avoid that, one should apply a weak N_2 flow, gradually increasing the flow until the water is completely evaporated.

Note 3: Typically, time needed to etch through a PMMA layer with 250nm thickness is around 3 minutes. However in order to get a sufficient undercut for dimers, the typical time required is around 6-7 minutes for particle sizes 100-170 nm. For trimers, the time should be increased to 8-9 minutes for particle sizes 100-150 nm. For bigger particle sizes 170-200 nm and even larger sizes up to 250 nm, the etching time should be increased up to 10-12 minutes.

5.2 Fabrication of nanoelliptical antennas.

Elliptical nanostructures with different aspect ratios (AR) between the symmetry axes can be fabricated by simply applying the steps (a-d) in figure 5.1 for PS beads deposition followed by angular evaporation of Cr mask. When the substrate is tilted during mask evaporation process, the PS bead will create an elliptical shadow (Figure 5.2a), which then will result in an elliptical mask.

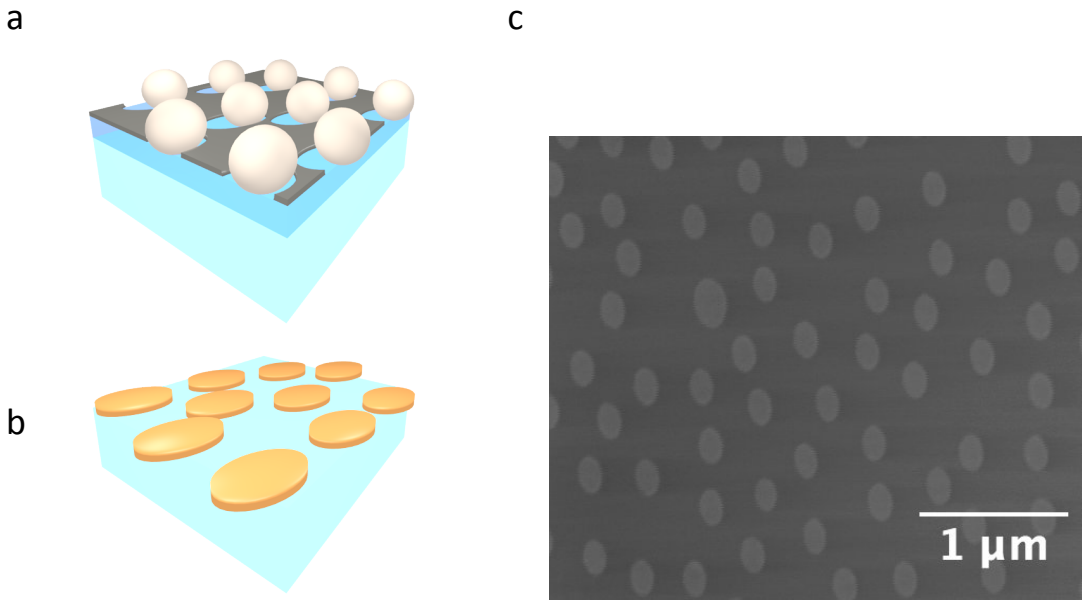

Figure 5.2. (a) Angular deposition of elliptical mask. (b) Nanoellipses fabricated by using elliptical mask. (c) SEM micrograph of Au ellipses with short axis 170 nm and aspect ratio 2.0.

After mask deposition, the process is similar to standard HCL procedure when the steps (f-i) in figure 5.1 are applied and the final structure will be a nanoellips (Figure 5.2b). The length of the short axis of this ellipse will always be equal to the diameter of the PS beads used in HCL process whereas the length of the long axis of the ellipse will be given by the degree of ellipticity, or AR, which is defined by the tilt angle and does not depend on the size of PS beads. For any size of PS beads, tilting the substrate by 45 degrees will result in aspect ration 1.4 meaning that the long axis of the ellipse is 1.4 times longer than the short axis, being 100 nm and 140 nm respectively for 100 nm PS beads. Tilting the substrate by 60 degrees will result in aspect ratio 2.0 (see SEM image on figure 5.2c), which is the highest AR that can be practically achieved by using this using method. Tilting at higher than 45 degrees angles is realized by using a tilted holder additionally to the tilt of the substrate.

5.3 Fabrication of nanodimer antennas.

Nanofabrication of more complex nanostructures such as dimers and trimers requires modification of the processes described in figure 5.1 but the steps (a-f) in figure 5.1 remain unmodified. When the PS beads are removed, O_2 plasma etching (Fig. 5.1g) needs to be applied for longer time to create a sufficient undercut in the PMMA layer (Figures 6.3a and 5.3b), which is facilitated by the anisotropic nature of dry etching. This undercut is crucial for angular evaporation, which is used to fabricate a nanoparticle dimer (Figure 5.3f) and a nanoparticle trimer (Figure 5.3h).

During evaporation of a metallic layer for the first nanoparticle, the substrate is kept normal to the direction of evaporation (Figure 5.3c) to produce a single nanoparticle (Figures 5.3c and 5.3d) and then tilted to produce a binary nanoparticle (Figures 5.3e and 5.3f). Alternatively, tilting the substrate to produce the first particle and then tilting the substrate in the opposite direction to produce the second particle gives the same result, which sometimes can be preferred because such a process requires a smaller tilt and thus a smaller undercut in PMMA. This protocol was used to produce the dimer nanorulers. The tilt and rotation are repeated 3 times with small increments in thickness (10 nm) to minimize the difference in particle sizes. Finally, lift-off of PMMA completes the fabrication procedure of a dimer nanoparticle (Figure 5.3f). The gap between the particles is tuned by

varying the evaporation angle, which in its turn depends on the size of the PS beads used in the process.

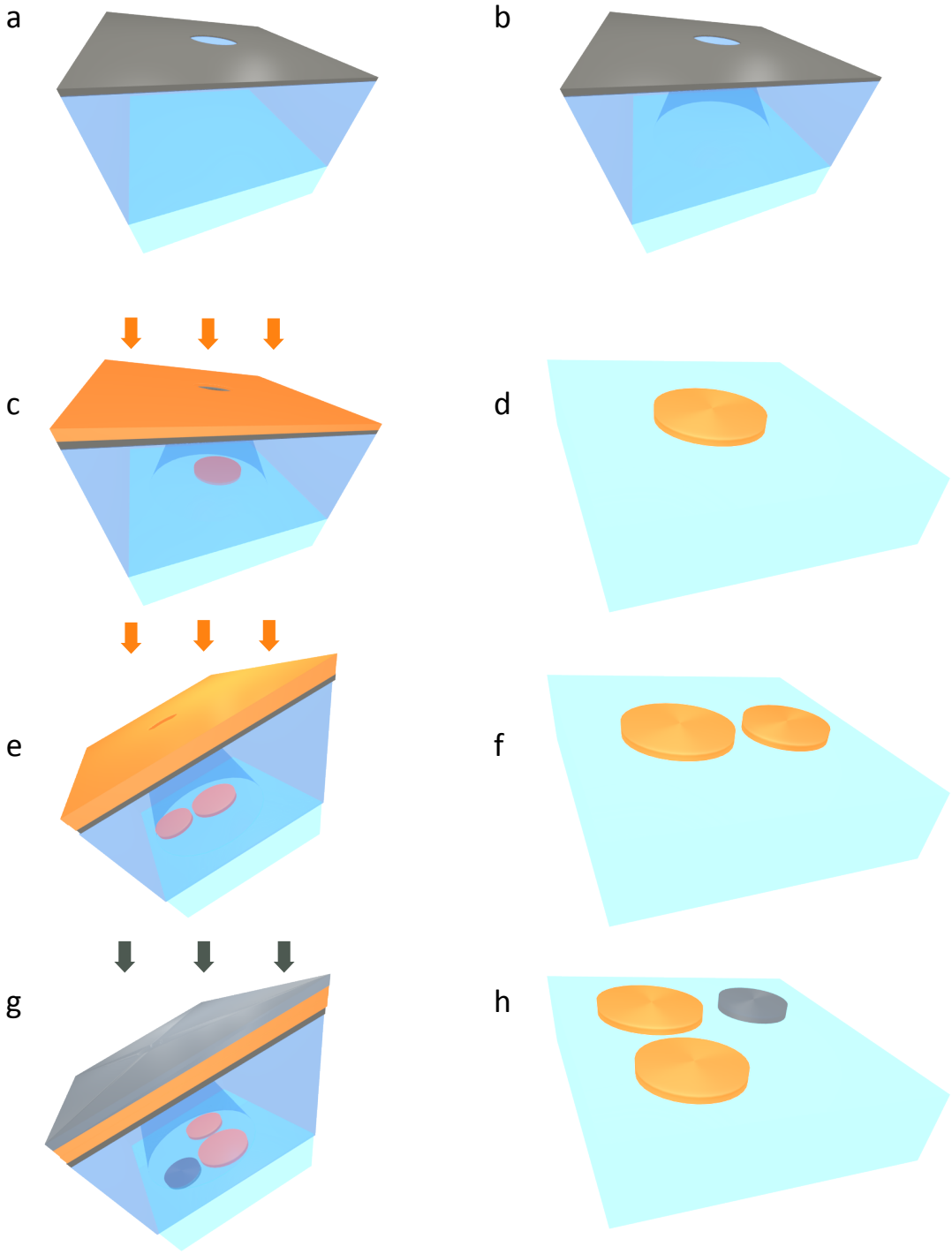

Figure 5.3. Nanofabrication of single nanodisks, nanodisk dimers and nanodisk trimers with HCL. (a) Hole-mask residing on PMMA layer. (b) Anisotropic O_2 plasma etching. (c) Deposition of single nanoparticle. (d) Single nanodisk. (e) Deposition of binary nanoparticle. (f) Nanodisk dimer. (g) Deposition of third nanoparticle. (h) Nanodisk trimer.

We use Ni and Co to fabricate magnetoplasmonic dimer nanorulers and Au to fabricate purely plasmonic reference nanorulers in Paper II. For the nanorulers with 150nm in diameter, the set of angles ($+16^0$ and -19^0) was used to achieve a 10 nm gap; ($+19^0$ and -19^0) was used to achieve a 20 nm gap and ($+21^0$ and -21^0) was used to achieve a 30 nm gap. HCL method combined with angular electron beam evaporation allows producing nanoparticle dimers with nicely controlled nanogap size. The micrographs of the nanorulers with several nanogap sizes are provided in Fig. 5.4. The limitation of HCL in producing dimer rulers with exceedingly large nanogaps (i.e., at 50 nm and above for nanoparticles with 150 nm in diameter) stems from the fact that the model nanofabricated rulers in our case can only be separated by the distance roughly twice the nanodisk diameter in the ruler. That is, at large nanogap sizes the inter-ruler distance becomes smaller than the nanogap itself. To bypass that effect, nanorulers with lower particle concentration can be used, however that will have a negative effect on the signals.

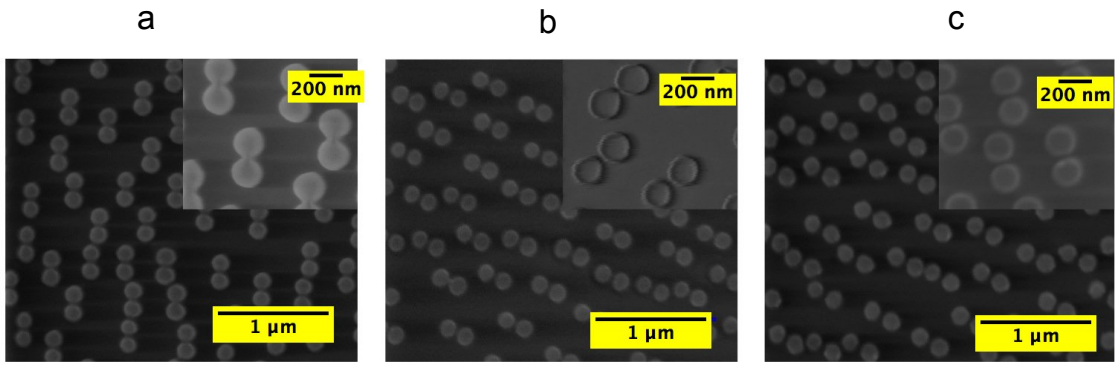

Figure 5.4. Scanning electron micrographs of magnetoplasmonic nanorulers made of Ni with (a) 10 nm nanogap, (b) 20 nm nanogap and (c) 30 nm nanogap fabricated with HCL.

5.4 Fabrication of nanotrimer antennas.

During evaporation of a metallic layer for the first nanoparticle in a trimer the substrate is first kept normal to the direction of evaporation (Fig. 5.3c), then tilted to produce a binary nanoparticle (Fig. 5.3e), and finally rotated by 90 degrees to deposit the third nanoparticle in the trimer (Figs. 5.3g and 5.3h). Trimer nanoantennas in Paper 3 were fabricated by using Au for the first and second nanoparticles and Ni for the third nanoparticle.

Due to the mask shrinking during the material deposition, the particles are produced with slightly different sizes so that the first particle is always bigger that the second, and the second particle is always bigger than the third particle. This also affects the gap in the Au-Ni pair but can be controlled by adjusting the tilt manually before the deposition starts. The cycle is repeated 3 times with small increments in thickness (10 nm steps at one cycle) in order to minimize the difference in particle size for some of the samples. The gap between the particles is tuned by varying the evaporation angle and can be controlled for any of the two pairs of particles in a trimer (Au-Au and Au-Ni, or both) with a high precision of ~5-10 nm. The micrographs of the trimer antennas with different structural parameters are provided in Fig. 5.5. In one of the samples (Figure 5.5a), the effect of hole-mask shrinking was intentionally used to produce a highly anisotropic sample with different particle sizes.

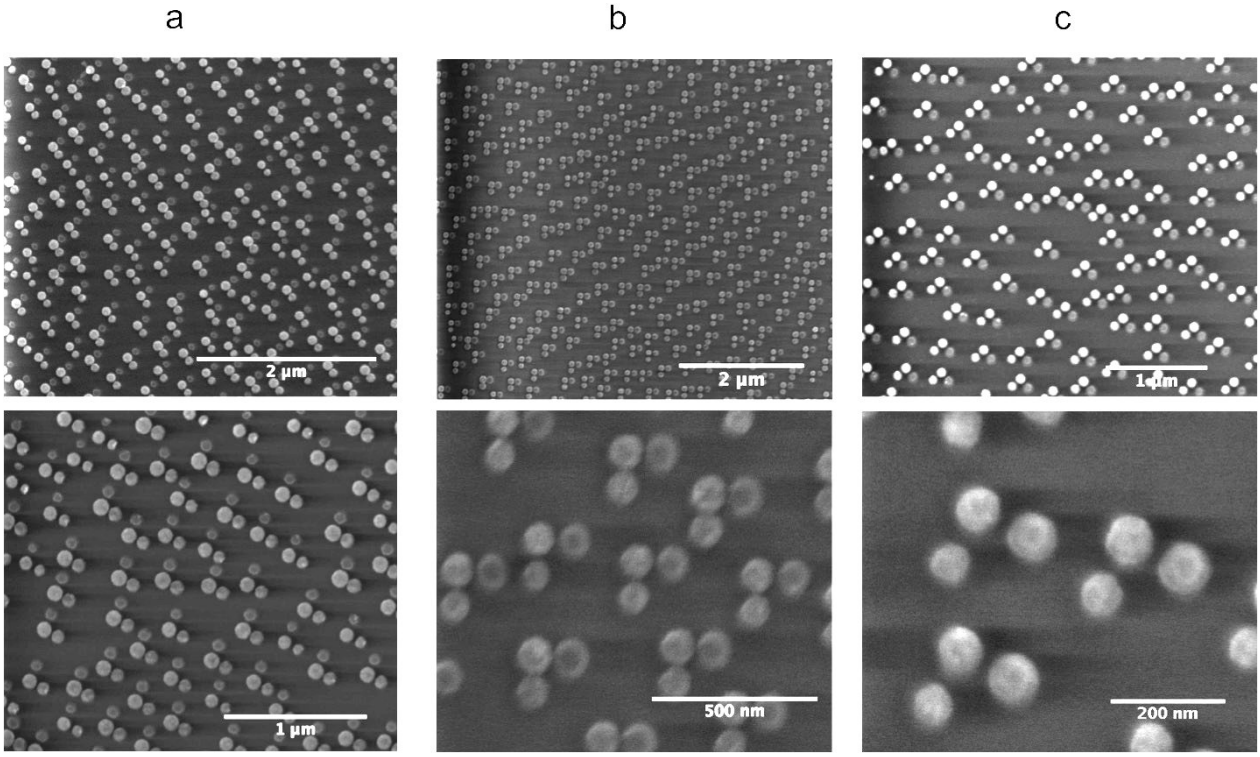

Figure 5.5. Scanning electron micrographs of magneto-chiral trimer nanoantennas with different structural parameters fabricated with HCL. (a) Nanoantennas with the highest variation in nanodisks sizes (diameters): Ni 70-90 nm, Au 100-126nm. Nanogap sizes in Au-Au pairs (Au particles have higher contrast) are 12 nm - 0 nm (overlapping), gap sizes in Ni-Au pairs are 16-21 nm. (b) Nanoantennas with nanodisks sizes Au 75- 115 nm, Au 85- 121 nm, Ni 87- 116 nm. Average gap sizes in Au-Au pairs are 10 nm - 0 nm (overlapping) and 5-10 nm- 0 nm (overlapping) in Ni-Au pairs. (c) Nanoantennas with nanodisks sizes Au 65-70

nm, Au 74-80 nm, Ni 85-90 nm. Average gap sizes in Au-Au pairs are 20 nm and 10-20 nm in Ni-Au pairs.

In principle, any choice of materials that can be deposited by PVD is possible to produce any other type of trimers. We demonstrate that in Paper 4, where we produced hybrid magneto-dielectric trimer surfaces made of two Si nanoparticles and the third nanoparticle made of ultrathin magnetic multilayers of Co and Au (Figure 5.6). In this work, the deposition of the two Si nanoparticles was done at much lower pressure below $\sim 2 \cdot 10^{-7}$ Torr to ensure that Si is pure and no oxides of Si has formed. The deposition of the third nanoparticle started with a bottom Au layer of 1.5 nm thickness. In the next step, a multilayer sandwiches (Co0.5nm/Au1.5nm) were repeatedly deposited with total number of multilayers (Co/Au) N=18. As the last step, a top layer of Au with 1.5 nm thickness was deposited.

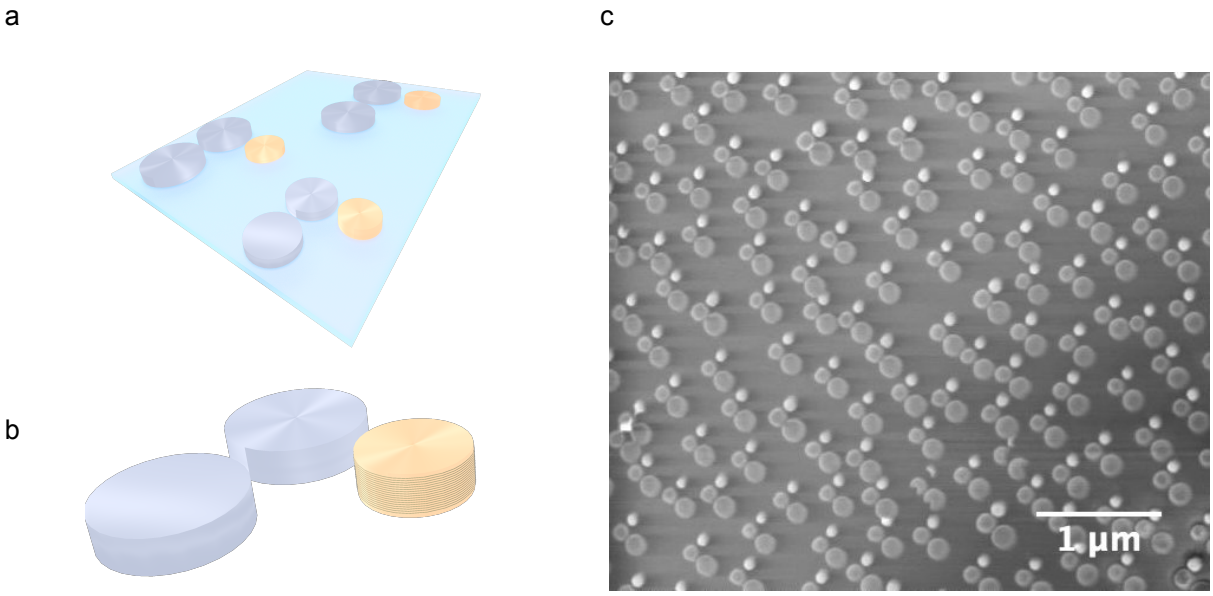

Figure 5.6 Hybrid magneto-dielectric nanotrimer surfaces. (a) A model of hybrid magneto-dielectric trimer surface. (b) Close-up of a single nanotrimer made of two Si nanoparticles and the third nanoparticle made of ultrathin magnetic multilayers of Co and Au. (c) SEM micrograph of a magneto-dielectric trimer surface.

6 Lock-in measurements with photoelastic modulator

6.1 Spectroscopic L-MOKE technique

A full description of Kerr effect requires measurement of both rotation θ_K and ellipticity ϵ_K. The experimental set-up used in Paper 1 and Paper 2 is based on the polarization-modulation technique [66] and includes a photo-elastic modulator (PEM). The spectroscopic magneto-optic response of the magnetoplasmonic nanorulers is measured with a home-built L-MOKE set-up at an angle of light incidence of 25°, sketched in Figure 6.1.

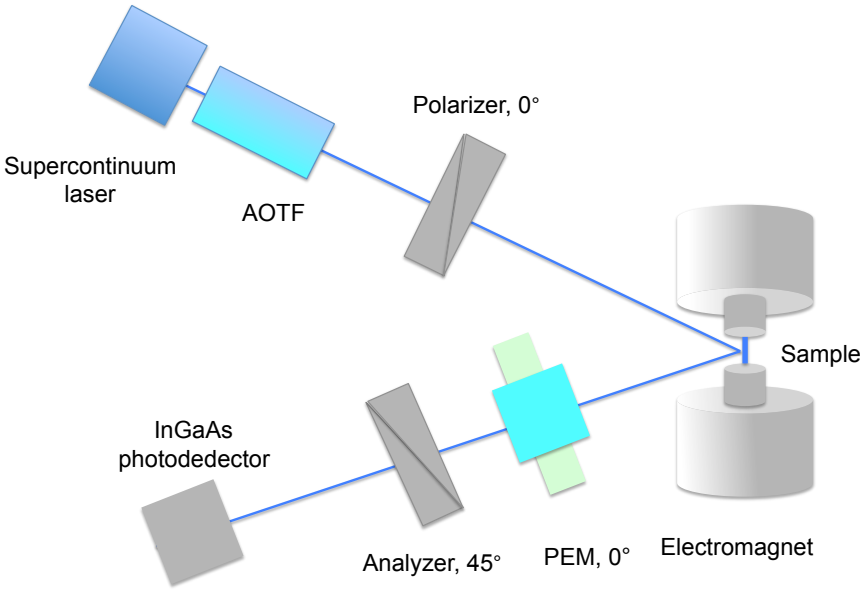

Figure 6.1. Schematic representation of spectroscopic L-MOKE set-up, where a straight line shows the light path.

The light is generated by ultra-broadband supercontinuum laser source (Fianium, Ltd.), which can potentially emit a radiation in the wavelength range from 450 nm to 2000 nm with a maximum power output about 5W. The output from the laser is connected to dual acousto-optic tunable filter (AOTF), which is used to filter-out a particular wavelength. AOTF consists of two piezoelectric crystals, designed to work in two optical regions: the visible range 450 nm- 600 nm and visible- near-infrared range 600 nm-1100 nm. A

monochromatic laser beam from AOTF is sent through a multimode optical fiber with a collimating lens. This laser beam passes a rotatable Glan-Thompson polarizer (Newport), which can be set to provide either p-polarized or s-polarized light. The sample is placed between in a gap of the ferrite electromagnet so that the magnetization is induced in the sample plane and parallel to the plane of light incidence. The magnetic field of 2500 kOe of both polarities is applied in order to ensure the complete magnetization saturation of the samples. When linearly polarized laser beam reflects from a magnetized sample surface, the rotation θ_K and ellipticity ϵ_K are introduced. The reflected beam passes through a photo-elastic modulator (PEM-90, Hinds instruments) which provides a polarization modulation at frequency $\omega = 50\ kHz$. After passing a second Glan-Thompson polarizer, or analyzer, set to 45°, the light is detected by InGaAs avalanche photodetector (Thorlabs). The signal from the photodetector is sent to two lock-in amplifiers (Standford Research Systems, SR830DSP), which measure the components of the signal modulated at the ω ($1f$) and 2ω ($2f$) [66] [67]. The DC component of the signal is measured by highly sensitive digital multimeter (Keithley, 2400).

The analytical description of the operation of L-MOKE technique is presented below. The intensity of light arriving at the photodetector may be written as [68]:

$$I(t) = I_0(1 + 2\theta_k \cos(A_0\omega t) - 2\epsilon_k \sin(A_0\omega t)), \tag{1}$$

where I_0 represents the DC intensity, $\omega = 2\pi f$ is the angular frequency of PEM oscillations, A_0 is the retardation amplitude of the PEM, θ_K is Kerr rotation and ϵ_K is Kerr ellipticity. Using a Fourier series expansion and keeping only the first three terms gives:

$$I(t) \cong I_0\left(\overbrace{1 + 2\theta_k J_o(A_o)}^{V_{DC}} - \overbrace{4\epsilon_k J_1(A_0)\sin\omega t}^{V_{1f}} + \overbrace{4\theta_k J_2(A_0)\cos(2\omega t)}^{V_{2f}}\right), \tag{2}$$

with J being Bessel functions. Here the first two terms are the parts of DC signal, when the second term can be neglected if the retardation A_o is set to 2.405 radians, in which case J_o=0. There are three voltages measured in the L-MOKE experiment: V_{DC}, V_{1f} and V_{2f}. It is convenient to express Kerr rotation θ_K and Kerr ellipticity ϵ_K as a ratio of the AC term to the DC term in order to avoid the influence of fluctuations in the light intensity during the experiment. The final expressions are, therefore, given by:

$$\theta_k = \frac{\sqrt{2}}{4J_2}\frac{V_{2f}}{V_{DC}} \tag{3}$$

$$\epsilon_k = \frac{\sqrt{2}}{4J_1}\frac{V_{1f}}{V_{DC}} \tag{4}$$

6.2 Circular differential transmission and its magnetic modulation

6.2.1 Experimental set-up

The experimental set-up used to measure the circular differential transmission (CDT) in Paper 3 is schematically presented in Figure 6.2. We use a supercontinuum white laser source (Fianium®) in optical wavelength region 450-1100 nm to perform the spectroscopic measurements of CDT. The output from the laser is supplied by multimode optical fiber and collimated in a 5 mm beam that is sent then to Glan-Thompson polarizer set at -45 degrees. The beam polarization is further controlled by a photoelastic modulator (PEM) with a peak retardation set to 0.25 wavelengths, modulating the light polarization between LCP and RCP at PEM frequency (1f) 50kHz. The transmitted intensity is recorded by a photodetector and the signal is fed to a lock-in amplifier locked to the PEM frequency 50kHz.

The magnetically tunable CDT spectra are recorded via an externally applied DC magnetic field at magnetic saturation H and –H with the magnitude 3kOe (~0.3T). The experimental set-up is equivalent to the set-up used in CDT measurements presented in Fig. 6.2 with only difference that now the sample is positioned between the poles of the electromagnet (Fig. 6.3) where the magnetic field is homogeneous. Because the circulating currents generate heat, it is important that the magnet is supplied with water-cooling system during the measurements.

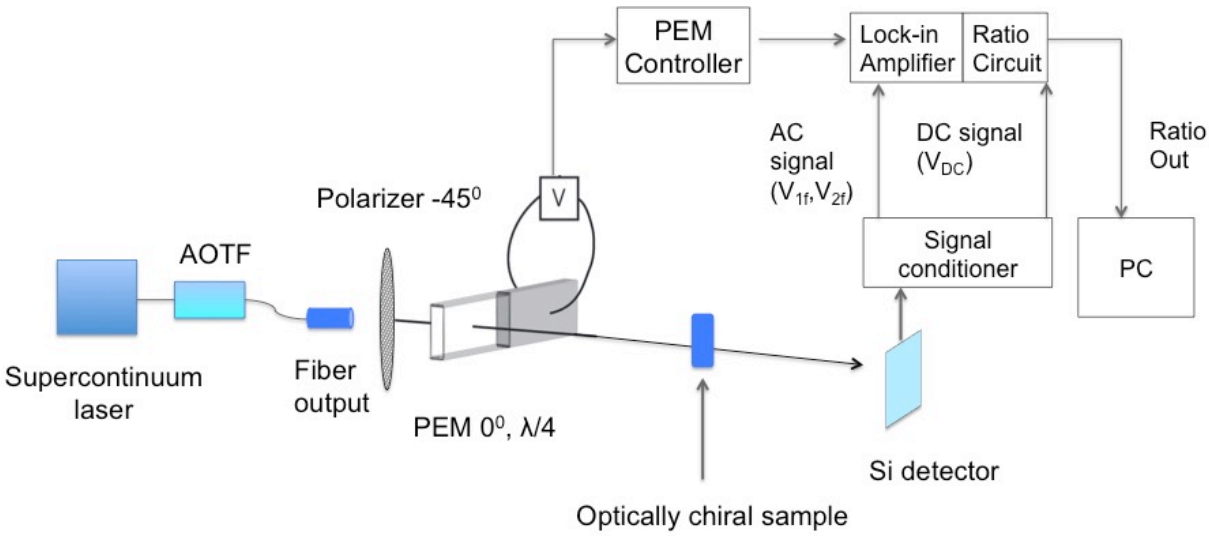

Figure 6.2. Schematic representation of the experimental set-up used in measurements of circular differential transmission.

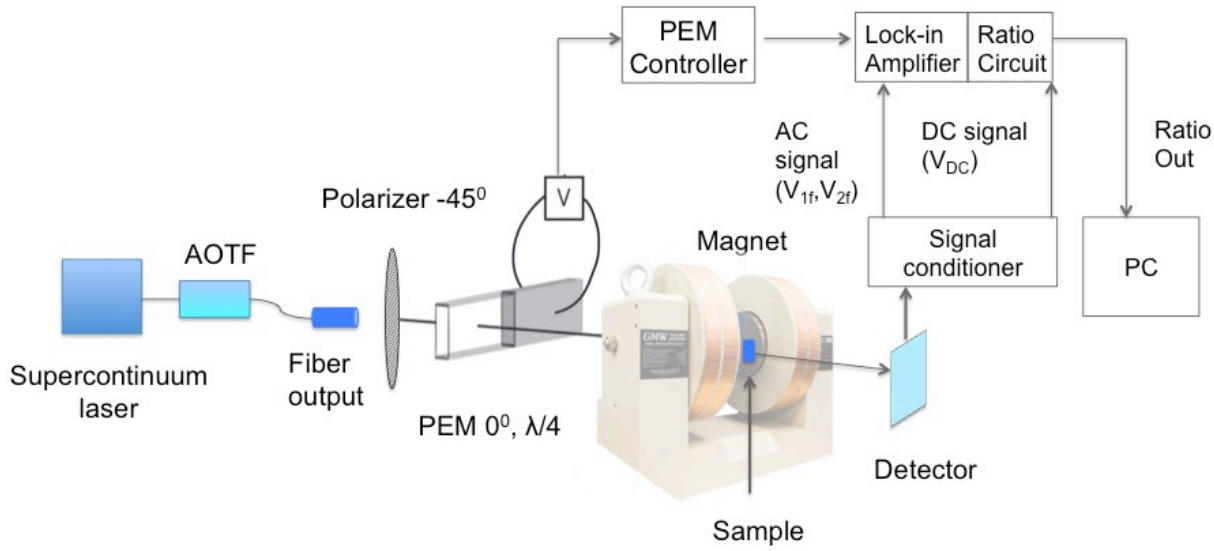

Figure 6.3. Experimental set-up for measurements of magnetically modulated circular differential transmission.

After the PEM, the light beam is modulated between right- (RCP) and left circular polarization (LCP) at the modulator frequency (1f) (Figure 6.4). When the sample is optically chiral, i.e. absorbs and scatters right- and left circular polarization differently, the signal coming from the detector will have an AC component at 1f that is related to differential transmission of RCP and LCP, or CDT. Another method of measuring the CDT is to separately record the transmission spectra with RCP and LCP and make a subtraction.

However, the CDT is normally several orders of magnitude smaller than the transmission of RCP and LCP and it is extremely difficult to obtain pure circular light experimentally by using a quarter-wave plate, a Fresnel rhomb or other optical components that create light phase retardation. In such experiments one can not guarantee that the light becomes purely circular mainly for the reason that the phase retardation is not constant over a wide wavelength region, and also due to the difficulties of the alignment. The stability and dynamic range of these components cannot meet such a requirement of precise and constant phase retardation over big wavelength regions, therefore, PEM modulation is preferred in spectroscopic CDT measurements.

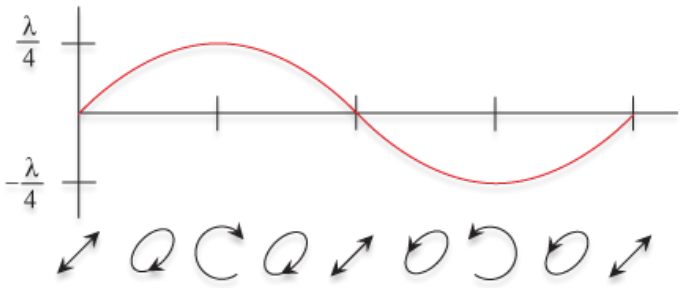

Figure 6.4. Modulation of light retardation and polarization between RCP and LCP at frequency 1f in photoelastic modulator. Adapted from the reference [69]

6.2.2 Introduction of Stokes vector

A common representation of Stokes vector is

$$S = \begin{bmatrix} S \\ Q \\ U \\ V \end{bmatrix} = \{S \quad Q \quad U \quad V\}, \tag{1}$$

where the elements of the Stokes vector are defined as:

$S \equiv$ Total intensity

$Q \equiv I_0 - I_{90} =$ Difference in intensities between horizontally and vertically linearly polarized components

$U \equiv I_{+45} - I_{-45}$ = Difference in intensities between linearly polarized components oriented at $+45^0$ and -45^0.

$V \equiv I_{RCP} - I_{LCP}$= Difference in intensities between right and left circularly polarized components.

6.2.3 Derivation of CDT from the time-varying intensity arriving at the photodetector with Stokes-Muller approach

The light from the fiber output becomes linearly polarized at -45^0 after the polarizer with the Stokes vector

$$S_{-45} = \begin{bmatrix} 1 \\ 0 \\ -1 \\ 0 \end{bmatrix}. \tag{1}$$

The linearly polarized light at -45^0 is then sent to PEM at 0^0 (Fig. 6.2), which is described by the Muller matrix

$$M(\delta) = \begin{bmatrix} 1 & 0 & 0 & 0 \\ 0 & 1 & 0 & 0 \\ 0 & 0 & \cos(\delta) & \sin(\delta) \\ 0 & 0 & -\sin(\delta) & \cos(\delta) \end{bmatrix}, \tag{2}$$

where $\delta = \delta_0 \sin \omega t$ is a retardation in radians generated on the PEM at a particular moment with angular velocity $\omega = 2\pi f$, and $f = 50\ kHz$.

When the linearly polarized at -45^0 light passes through the PEM with time-modulated retardation, the resulting Stokes vector of the beam emerging after PEM and incident on the sample will be

$$S_{PEM} = M(A) \times S_{-45} = \begin{bmatrix} 1 & 0 & 0 & 0 \\ 0 & 1 & 0 & 0 \\ 0 & 0 & \cos(\delta) & \sin(\delta) \\ 0 & 0 & -\sin(\delta) & \cos(\delta) \end{bmatrix} \times \begin{bmatrix} 1 \\ 0 \\ -1 \\ 0 \end{bmatrix} = \begin{bmatrix} 1 \\ 0 \\ -\cos(\delta) \\ \sin(\delta) \end{bmatrix}. \tag{3}$$

As expected, if the amplitude of the retardation of the PEM is chosen to be 0.25 wavelengths, that is equivalent to 1.57 radians, or $\pi/2$, the light becomes right-hand circularly polarized.

In order to determine the effect of a material exhibiting differential transmission of right and left circularly polarized light, the actual intensities I_{RCP} and I_{LCP} are needed. From the obtained Stokes vector we know that

$$I_{RCP} + I_{LCP} = I_0, \tag{4}$$

$$I_{RCP} - I_{LCP} = I_0 \sin\delta, \tag{5}$$

which yields the values

$$I_{LCP}/_{RCP} = \frac{I_0}{2}(1 \mp sin\ \delta) \tag{6}$$

and

$$I_0/_{90} = \frac{I_0}{2}(1 \pm cos\delta). \tag{7}$$

In direct analogy with circular dichroism (CD) in biochemical chiral systems, where CD is determined as a *differential absorption* for left- and right circularly polarized light, we define here the *circular differential transmission (*which accounts for both absorption and scattering*)* as $\Delta\mathfrak{E}_{CDT} = \mathfrak{E}_{LCP} - \mathfrak{E}_{RCP}$ with $\mathfrak{E}_{LCP}$ and $\mathfrak{E}_{RCP}$ being the extinctions for left- and right circularly polarized light and corresponding *Eulerian extinctions* ϵ_{LCP} and ϵ_{RCP} for our plasmonic chiral system.

The transmitted intensity after an optically chiral sample is related to the incident intensity as [70]

$$I = I_0 10^{-\mathfrak{E}} = I_0 e^{-\epsilon} \qquad \Longrightarrow \qquad \epsilon = \mathfrak{E}\ ln10 \approx 2.303\ \mathfrak{E}. \tag{8}$$

Eulerian differential extinctions are defined as $\epsilon_{LCP/RCP} = \bar{\epsilon} \pm \frac{1}{2}\Delta\epsilon$, where $\Delta\epsilon$ is the average of the two and $\Delta\epsilon$ is their difference.

The total intensity leaving an optically chiral sample and arriving at the photodetector is given by the sum of attenuated intensities of left- and right circularly polarized components [70]:

$$I(t) = I_{LCP}e^{-\epsilon_{LCP}} + I_{RCP}e^{-\epsilon_{RCP}} =$$

$$= \frac{I_0}{2}(1 - sin[\delta_0\, sin\omega t])e^{\bar{\epsilon}+\frac{1}{2}\Delta\epsilon} + \frac{I_0}{2}(1 + sin[\delta_0\, sin\omega t])e^{\bar{\epsilon}-\frac{1}{2}\Delta\epsilon} =$$

$$\Longrightarrow I(t) = I_0 e^{-\bar{\epsilon}}(1 + \Delta\epsilon J_1(\delta_0)\sin\omega t + \cdots), \tag{9}$$

where the *sine* function was replaced by the lowest frequency term in the Bessel function expansion Fourier series

$$\sin[\delta_0 \sin\omega t] = 2J_1(\delta_0)\sin\omega t + 2J_3(\delta_0)sin3\omega t + \cdots \tag{10}$$

and each exponential term containing $\Delta\epsilon$ was expanded in Tailor series and only lowest order term was retained.

6.2.4 Measurement of CDT and magnetically modulated CDT

The intensity arriving at the photodetector (Eq. 9 in 6.2.3) in a form of photon count generates a photocurrent, which is converted to time-varying AC voltage $V[t]$. This voltage consists of a constant DC component V_{DC} and components modulated at the frequency of PEM $V_\omega, V_{2\omega}, \ldots$:

$$\mathrm{V(t)} = V_0 + V_\omega \sin\omega t + V_{2\omega}\sin 2\omega t + \cdots. \tag{11}$$

The actual CDT, defined as *circular differential transmission* is proportional to the ratio of the AC term to the DC term:

$$\frac{V_\omega}{V_{DC}} = \Delta\epsilon\, J_1(\delta_0), \tag{11}$$

Finally, the CDT can be obtained experimentally as follows:

$$\Longrightarrow\ \Delta\mathfrak{E}_{CDT} = \mathfrak{E}_{LCP} - \mathfrak{E}_{RCP} = \frac{\sqrt{2}}{ln10\, J_1(\delta_0)}\frac{V_\omega}{V_{DC}} = \frac{\sqrt{2}}{2.303\, J_1(\delta_0)}\frac{V_\omega}{V_{DC}}, \tag{12}$$

where the voltage V_{DC} is a DC component of the signal and V_{ω} is a component measured at the fundamental first harmonic ω. The factor of $\sqrt{2}$ accounts for rms voltage in the lock-in amplifier whereas the theory is written in terms of peak voltage or voltage amplitude.

The retardation we use in our experiment is a quarter wavelength, 0.25λ, or 1.57 rad with the Bessel function $J_1(1.57) = 0.567$.

As it can be seen from the Equation 12, the choice of the PEM phase is not necessary 0.25λ and can any phase retardation δ_0 of the PEM, except for the one that causes $J_1(\delta_0)$ to equal zero, can be used to extract the CD signal. For example, the maximal experimental signal can be obtained for the phase $\delta_0 = 0.587\,\pi$ (106°) for which the Bessel function $J_1(\delta_0)$=0.582 reaches its maximum [70]. This flexibility in the choice of PEM phase is important for the design of measurements when many parameters can be extracted from the same experiment.

7 Summary and Outlook

In this last chapter I will give a brief summary of the most important findings presented in the papers included in this thesis and end this chapter with a brief outlook.

In Paper 1, we introduce magnetoplasmonics, the combination of nanomagnetism and plasmonics, as a promising route for bringing future active photonic devices to the nanoscale. We produce highly tunable active magnetoplasmonic elements that enable active polarization control via magneto-optical Kerr and Faraday rotation. We demonstrate the role of spin-orbit coupling in magneto-optical response and further introduce the generalized analytical expressions via polarizabilities of magneto-optical Kerr effect (MOKE) in three commonly employed configurations, such as longitudinal (L-MOKE), polar (P-MOKE) and transverse (T-MOKE). These expressions, or the 'design rules', are necessary to engineer 2D and 3D magnetoplasmonic nanoantennas with highest tunability and broadband control of light polarization over the visible and near-infrared spectral regions in future magneto-optical active devices.

In Paper 2, we add magnetoplasmonics to the ultrasensitive optical measurements of the nanoscale distances. Plasmon rulers are an emerging concept in which the strong near-field coupling of plasmon nanoantenna elements is employed to obtain structural information at the nanoscale. We develop a new type of a magnetic field-activated plasmon ruler that reports nanogap distances via Kerr polarization rotation. We combine nanoplasmonics and nanomagnetism to conceptualize a magnetoplasmonic dimer nanoantenna that would be able to report nanoscale distances while optimizing its own spatial orientation with the figure-of-merit substantially exceeding the one of traditional plasmon rulers. The latter constitutes an active operation, in which a dynamically optimized optical response per measured unit length allows for the measurement of small and large nanoscale distances with about two orders of magnitude higher precision than current state-of-the-art plasmon rulers.

Paper 3 shows how magnetoplasmonics can be successfully combined with chiroptics. We produce a novel type of ultra-thin surface that delivers the dynamic magnetic modulation of the far-field chiroptical response, exceeding 100% in the tunability, in the visible and near-infrared spectral ranges. In this work, we design and nanofabricate optically chiral 2D

composite nanotrimer antennas consisting of noble and ferromagnetic materials, where, despite of structural symmetry, the chiroptical response is achieved via materials combination. We demonstrate a large magnetic tunability of chiral differential transmission that is a result of the interplay between the phases of dipoles, excited in a bimetallic nanotrimer nanoantenna. We theoretically describe the origin of chiroptical effects in terms of simple coupled-dipole model and perform the detailed analysis of this new type of chiral systems via numerically calculated near-field and far-field response with and without applied magnetic field. Finally, we propose that, by adding small design modifications, the developed here magnetoplasmonic surfaces would readily reach the speed for the magnetically induced switching up to 10 GHz over the visible and near-IR spectral ranges while maintaining the exceptionally large tunability range of up to 100-150%.

Paper 4 has the ambition to demonstrate that a GHz magnetic modulation of far-field optical response can be practically realized in hybrid magneto-dielectric nanoantennas. Here we produced optically chiral highly transparent magneto-dielectric nanotrimer antennas consisting of silicon nanodisks and a combination of ferromagnetic (Co) and noble (Au) metals as a multilayer nanodisk stack. We use the same strategy as in Paper 3 (the materials asymmetry) to produce the chiroptical response in a close-to-symmetric nanotrimer. On the one side, silicon nanoantenna elements provide distinct Mie optical resonances with low losses and with high compatibility with existing complementary metal– oxide–semiconductor (CMOS) technology. On the other side, the geometry of metallic multilayer is motivated by a requirement of very low magnetic saturation field, needed for the GHz modulation, and is enabled by a perpendicular magnetic anisotropy, a well-studied phenomenon in magnetism. These hybrid nanoantennas, operating in visible spectrum and allowing a real-time and fast control of the fundamental properties of light, are envisioned to become the future elements for high-speed nanophotonic devices.

Outlook

We are now moving towards planar optical elements that operate beyond the diffraction limit and are built on single layer of phase shifting nanoantennas [71]. Plasmonic and all-dielectric optical materials, structured at the nanoscale, prove the capacity to replace the conventional refractive optics and offer all functionalities, required for practical realization of planar optical devices, e.g. lenses [72], holograms, beam deflectors [73] and polarizing interfaces [71]. Reconfigurable optical devices based on transition-metal oxides [74], [75] and silicon devices that control the phase of light [76] and convert linearly polarized light into circularly polarized light [77] are now very active topics in photonics. Magnetoplasmonic antennas with customized design would provide a valuable functionality for such applications, provided that the absorption losses are minimized and the compatibility with existing CMOS technology is assured. For that, one needs to build a hybrid system where low-loss efficient light scatterers are combined with elements that are responsive to magnetic fields.

One of the critical parameters for the real-time tunable plasmonic surfaces is the speed of operation. So far reported the slow-tuned systems reach significant changes of the tuned parameter (c.f., tuning the transmission [78-82], absorption [79], reflection [78, 79, 82] or CD [39, 80, 83]) at the expense of the operation speed and the prospect of integration and manufacturing simplicity. The fast-tuned plasmonic systems at MHz[80, 82] or the all-optically (i.e., THz) tuned systems [78, 79], conversely, suffer from the small tunability range. With the present nanoantennas the operation speed, in practice, is solely limited by the field-induced magnetization switching in a ferromagnetic element. Generally, the magnetization process is described by Landau-Lifshitz-Gilbert dynamic equation [84] where the damping factor, being large for ferromagnets, sets the fundamental limit for magnetization switching speed, which is typically in the order of 1 ns. However, the application of specifically shaped magnetic field pulses allows reaching time scales of ~100 ps [85]. Thereby, with the currently commercially available sources of the fast-modulated magnetic fields [86] we foresee that the developed here magnetoplasmonic surfaces would readily reach the ultimate speed for magnetically induced switching up to 10 GHz over the visible and near-IR spectral ranges while maintaining the exceptionally large tunability range of up to 100-150%.

Acknowledgements

Our group has been growing and evolving since I started my PhD on the 1st of August, 2012 and it was amazing to be a part of this evolution. I started in magnetoplasmonics but have been broadened my horizons with new fields where we combine magnetoplasmonics with chiral plasmonics and all-dielectric antennas. This thesis is a collection of my research and it is also a reflection of my growth as a scientist.

I am grateful to meet many good people during my journey and here I would like to thank the ones who have made this thesis possible:

First of all, my supervisor and the group leader, Alexander Dmitriev- thank you for providing me the opportunity to be a PhD student in your small but powerful group, for all inspiring and daring ideas and passion in science you always share, for your valuable guidance and always being available no matter where you are.

Esteban - I am very happy that we became colleagues during last 1.5 years of my PhD! Thank you for teaching me Spanish and Lumerical, and for all nice discussions about physics and life ☺ Thank you for being my best office mate and my friend.

Tua- You are such a nice person to work together, thank you for all your precious advices, help with LabView, amazing discussions and all lunches we ate together ☺

Paolo Vavassori and Nicolò Maccaferri- thank you for our nice collaboration and teamwork and for sharing your huge knowledge in magnetism and magneto-optics. Nicolò- thank you for kindly providing all analytical models and numerical calculations used in this thesis, and for your help with setting up the experiments for the measurement of chiroptical transmission during your visit here in Göteborg.

Clean room engineers Henrik Frederiksen and Mats Hagberg- I am grateful for all your help with evaporation tools in the cleanroom and always being nice and helpful. I am hugely thankful to Henrik, who helped me to practically realize all challenging nanofabrication ideas, for his patience, being always available and for sharing his knowledge in material science.

Kristof Lodewijks- thank you for introducing me to MOKE and helping out with ellipsometry measurements, and also for sharing your huge experience on nanofabrication, optics and plasmonics.

Randy K. Dumas- thank you for introducing me to alternating gradient magnetometry (AGM), for providing me high-quality magnetic films and for sharing your broad knowledge on nanomagnetism and magnetic materials.

Addis Mekonnen –thank you for all exciting discussions and sharing your passion in physics, for helping me out with measurements and for sharing your expertise in magnetism and optics.

Vladimir Miljković- thank you for introducing me to HCL and nanofabrication of dimers. Gülis Zengin-thank you for introducing me to scanning electron microscopy. Virginia Claudio- thank you for introducing me to ion beam milling. Mojtaba, Yuli, Masoumeh, Martina, Mohammad and Afshin in Johan Åkerman's group for being nice lab mates and floor neighbors.

My family: my parents for their endless love, care and support through my life, and my parents-in law, Ann-Marie and Hasse - it's a great pleasure in being a part of your family; Jakob for always being by my side.

Finally, I would like to acknowledge the Swedish Foundation for Strategic Research (SSF) Future Research Leader Grant.

Bibliography

1. Maier, S.A., *Plasmonics : fundamentals and applications*. 2007, New York: Springer. xxiv, 223 p.

2. Maier, S.A., *Plasmonics: Fundamentals and Applications.* 2007.

3. Gaponenko, S.V., *Introduction to nanophotonics*. 2010, Cambridge: Cambridge University Press. xviii, 463 s.

4. Armelles, G., et al., *Magnetoplasmonics: Combining Magnetic and Plasmonic Functionalities.* Advanced Optical Materials, 2013. **1**(1): p. 10-35.

5. Armelles, G. and A. Dmitriev, *Focus on magnetoplasmonics.* New Journal of Physics, 2014. **16**(4): p. 045012.

6. Temnov, V.V., et al., *Active magneto-plasmonics in hybrid metal–ferromagnet structures*. Nature Photonics, 2010. **4**(2): p. 107-111.

7. Belotelov, V.I., et al., *On surface plasmon polariton wavepacket dynamics in metal-dielectric heterostructures.* J Phys Condens Matter, 2010. **22**(39): p. 395301.

8. Temnov, V.V., *Ultrafast acousto-magneto-plasmonics.* Nature Photonics, 2012. **6**(11): p. 728-736.

9. Temnov, V.V., et al., *Femtosecond nonlinear ultrasonics in gold probed with ultrashort surface plasmons.* Nat Commun, 2013. **4**: p. 1468.

10. Pohl, M., et al., *Tuning of the transverse magneto-optical Kerr effect in magneto-plasmonic crystals.* New Journal of Physics, 2013. **15**(7): p. 075024.

11. Vasily V Temnov, I.R., Thomas Pezeril, Denys Makarov, Denis Seletskiy, Alexey Melnikov and Keith A Nelson, *Towards the nonlinear acousto-magneto-plasmonics.* Journal of Optics, 2016. **18**(9).

12. Gonzalez-Diaz, J.B., et al., *Plasmonic Au/Co/Au nanosandwiches with enhanced magneto-optical activity.* Small, 2008. **4**(2): p. 202-5.

13. Maccaferri, N., et al., *Tuning the Magneto-Optical Response of Nanosize Ferromagnetic Ni Disks Using the Phase of Localized Plasmons.* Physical Review Letters, 2013. **111**(16).

14. Bonanni, V., et al., *Designer magnetoplasmonics with nickel nanoferromagnets.* Nano Lett, 2011. **11**(12): p. 5333-8.

15. Zubritskaya, I., et al., *Active magnetoplasmonic ruler.* Nano Lett, 2015. **15**(5): p. 3204-11.

16. Maccaferri, N., et al., *Ultrasensitive and label-free molecular-level detection enabled by light phase control in magnetoplasmonic nanoantennas.* Nat Commun, 2015. **6**: p. 6150.

17. Maksymov, I.S., *Magneto-plasmonic nanoantennas: Basics and applications.* Reviews in Physics, 2016. **1**: p. 36-51.

18. Canet-Ferrer, J., et al., *Hybrid magnetite–gold nanoparticles as bifunctional magnetic–plasmonic systems: three representative cases.* Nanoscale Horiz., 2017. **2**(4): p. 205-216.

19. Zhang, M., et al., *High-strength magnetically switchable plasmonic nanorods assembled from a binary nanocrystal mixture.* Nat Nanotechnol, 2017. **12**(3): p. 228-232.

20. Stipe, B.C., et al., *Magnetic recording at 1.5 Pb m−2 using an integrated plasmonic antenna.* Nature Photonics, 2010. **4**(7): p. 484-488.

21. Griffiths, D.J., *Introduction to electrodynamics*. 3rd ed. 1999, Upper Saddle River, N.J.: Prentice Hall. xv, 576 p.

22. Novotny, L. and B. Hecht, *Principles of nano-optics*. 2006, Cambridge ; New York: Cambridge University Press. xvii, 539 p.

23. Hecht, E., *Optics*. 4. ed. 2002, San Francisco, Calif.: Addison Wesley. 698 s.

24. Johnson, P.B. and R.W. Christy, *Optical Constants of the Noble Metals.* Physical Review B, 1972. **6**(12): p. 4370-4379.

25. Bohren, C.F. and D.R. Huffman, *Absorption and scattering of light by small particles*. 1983, New York: Wiley. xiv, 530 p.

26. Nordlander, P.O., C.; Prodan, E.; Li, K.; Stockman, M. I. , *Plasmon Hybridization in Nanoparticle Dimers.* Nano Letters, 2004. **4**: p. 899–903.

27. Prodan, E., et al., *A hybridization model for the plasmon response of complex nanostructures.* Science, 2003. **302**(5644): p. 419-22.

28. Reinhard, B.M., et al., *Use of plasmon coupling to reveal the dynamics of DNA bending and cleavage by single EcoRV restriction enzymes.* Proc Natl Acad Sci U S A, 2007. **104**(8): p. 2667-72.

29. Sonnichsen, C., et al., *A molecular ruler based on plasmon coupling of single gold and silver nanoparticles.* Nat Biotechnol, 2005. **23**(6): p. 741-5.

30. Hill, R.T.M., J. J.; Hucknall, A.; Wolter, S. D.; Jokerst, N. M.; Smith, D. R.; Chilkoti, A., *Plasmon Ruler with Angström Length Resolution.* ACS Nano 2012. **6**: p. 9237–9246.

31. Prashant, K.J.H., W.; A. El-Sayed, M. , *On the Universal Scaling Behavior of the Distance Decay of Plasmon Coupling in Metal Nanoparticle Pairs: A Plasmon Ruler Equation.* Nano Letters, 2007. **7**: p. 2080–2088.

32. Na Liu, L.H., M.; Weiss, T.; Alivasatos, A. P.; Giessen, H., *Three-Dimensional Plasmon Rulers.* Science, 2011. **332**: p. 1407–1410.

33. Rechberger, W., et al., *Optical properties of two interacting gold nanoparticles.* Optics Communications, 2003. **220**(1-3): p. 137-141.

34. Wang, J.B., S. V.; Wang, H.; Reinhard, B. M., *Illuminating Epidermal Growth Factor Receptor Densities on Filopodia through Plasmon Coupling.* ACS Nano 2011. **5** p. 6619–6628.

35. Anker, J.N.H., W. P.; Lyandres, O.; Shah, N. C.; Zhao, J.; Van Duyne, R. P. , *Biosensing with plasmonic nanosensors.* Nature Materials, 2008. **7** p. 442–452.

36. Sheikholeslami, S., et al., *Coupling of optical resonances in a compositionally asymmetric plasmonic nanoparticle dimer.* Nano Lett, 2010. **10**(7): p. 2655-60.

37. Acimovic, S.S.K., M. P.; González, M. U.; Quidant, R. , *Plasmon Near-Field Coupling in Metal Dimers as a Step toward Single-Molecule Sensing.* ACS Nano 2009. **3**: p. 1231–1237.

38. Gunnarsson, L.R., T.; Prikulis, J.; Kasemo, B.; Käll, M.; Zou, S.; Schatz, G. C. , *Confined Plasmons in Nanofabricated Single Silver Particle Pairs: Experimental Observations of Strong Interparticle Interactions.* J. Phys. Chem. B. , 2005. **109** p. 1079–1087.

39. Kuzyk, A., et al., *Reconfigurable 3D plasmonic metamolecules.* Nat Mater, 2014. **13**(9): p. 862-6.

40. Zvezdin, A.K. and V.A. Kotov, *Modern magnetooptics and magnetooptical materials.* Studies in condensed matter physics. 1997, Philadelphia, Pa.: Institute of Physics Pub. xviii, 386 s.

41. Faraday, M., *Experimental Researches in Electricity. Nineteenth Series.* Philosophical Transactions Royal Society London, 1846. **136**.

42. Smith, D.A. and K.L. Stokes, *Discrete dipole approximation for magneto-opticalscattering calculations.* Optics Express, 2006. **14**(12): p. 5746-5754.

43. Xia, T.K., P.M. Hui, and D. Stroud, *Theory of Faraday rotation in granular magnetic materials.* Journal of Applied Physics, 1990. **67**(6): p. 2736.

44. Chen, J., et al., *Plasmonic nickel nanoantennas.* Small, 2011. **7**(16): p. 2341-7.

45. Sepúlveda, B., et al., *Plasmon-Induced Magneto-Optical Activity in Nanosized Gold Disks.* Physical Review Letters, 2010. **104**(14).

46. Pineider, F., et al., *Circular magnetoplasmonic modes in gold nanoparticles.* Nano Lett, 2013. **13**(10): p. 4785-9.

47. Banthi, J.C., et al., *High magneto-optical activity and low optical losses in metal-dielectric Au/Co/Au-SiO(2) magnetoplasmonic nanodisks.* Adv Mater, 2012. **24**(10): p. OP36-41.

48. de Sousa, N., et al., *Interaction effects on the magneto-optical response of magnetoplasmonic dimers.* Physical Review B, 2014. **89**(20).

49. Armelles, G., et al., *Mimicking electromagnetically induced transparency in the magneto-optical activity of magnetoplasmonic nanoresonators.* Optics Express, 2013. **21**(22): p. 27356.

50. Gonzalez-Diaz, J.B., et al., *Cobalt dependence of the magneto-optical response in magnetoplasmonic nanodisks.* Applied Physics Letters, 2010. **97**(4): p. 043114.

51. Maccaferri, N., et al., *Effects of a non-absorbing substrate on the magneto-optical Kerr response of plasmonic ferromagnetic nanodisks.* physica status solidi (a), 2014. **211**(5): p. 1067-1075.

52. Maccaferri, N., et al., *Polarizability and magnetoplasmonic properties of magnetic general nanoellipsoids.* Opt Express, 2013. **21**(8): p. 9875-89.

53. Lodewijks, K., et al., *Magnetoplasmonic design rules for active magneto-optics.* Nano Lett, 2014. **14**(12): p. 7207-14.

54. Maoz, B.M., et al., *Amplification of chiroptical activity of chiral biomolecules by surface plasmons.* Nano Lett, 2013. **13**(3): p. 1203-9.

55. Bliokh, K.Y., et al., *Spin–orbit interactions of light.* Nature Photonics, 2015. **9**(12): p. 796-808.

56. Nir Shitrit, I.Y., Elhanan Maguid, Dror Ozeri, Dekel Veksler, Vladimir Kleiner, Erez Hasman, *Spin-Optical Metamaterial Route to Spin-Controlled Photonics.* Science, 2013. **340**.

57. Xiao, S., et al., *Helicity-Preserving Omnidirectional Plasmonic Mirror.* Advanced Optical Materials, 2016. **4**(5): p. 654-658.

58. Valev, V.K., et al., *Chirality and chiroptical effects in plasmonic nanostructures: fundamentals, recent progress, and outlook.* Adv Mater, 2013. **25**(18): p. 2517-34.

59. Bettina Frank, X.Y., Martin Schäferling, Jun Zhao, Sven M. Hein, Paul V. Braun and Harald Giessen, *Large-Area 3D Chiral Plasmonic Structures.* ACS Nano, 2013. **7**(7): p. 6321–6329.

60. Gibbs, J.G., et al., *Plasmonic nanohelix metamaterials with tailorable giant circular dichroism.* Applied Physics Letters, 2013. **103**(21): p. 213101.

61. Song, C., et al., *Tailorable plasmonic circular dichroism properties of helical nanoparticle superstructures.* Nano Lett, 2013. **13**(7): p. 3256-61.

62. Khanikaev, A.B., et al., *Experimental demonstration of the microscopic origin of circular dichroism in two-dimensional metamaterials.* Nat Commun, 2016. **7**: p. 12045.

63. Schnell, M., et al., *Real-Space Mapping of the Chiral Near-Field Distributions in Spiral Antennas and Planar Metasurfaces.* Nano Lett, 2016. **16**(1): p. 663-70.

64. Banzer, P., et al., *Chiral optical response of planar and symmetric nanotrimers enabled by heteromaterial selection.* Nat Commun, 2016. **7**: p. 13117.

65. Fredriksson, H., et al., *Hole–Mask Colloidal Lithography.* Advanced Materials, 2007. **19**(23): p. 4297-4302.

66. Vavassori, P., *Polarization modulation technique for magneto-optical quantitative vector magnetometry.* Applied Physics Letters, 2000. **77**(11): p. 1605.

67. Kemp, J.C., *Polarized Light and its Interaction with Modulating Devices.* HINDS International, Inc., 1987.

68. Oakberg, T., *Magneto-optic Kerr Effect application note*, in *Hinds Instruments*. 2010.

69. Oakberg, T., *Linear and Circular Dichroism.* Hinds Instruments.

70. B.A Wallace and R.W. Janes, *Modern Techniques for Circular Dichroism and Synchrotron Radiation Circular Dichroism Spectroscopy*. 2009: IOS Press 243.

71. Genevet, P., et al., *Recent advances in planar optics: from plasmonic to dielectric metasurfaces.* Optica, 2017. **4**(1): p. 139.

72. Mohammadreza Khorasaninejad, W.T.C., Robert C. Devlin, Jaewon Oh, Alexander Y. Zhu, Federico Capasso, *Metalenses at visible wavelengths: Diffraction-limited focusing and subwavelength resolution imaging.* Science, 2016. **352**(6290).

73. Zhou, Z., et al., *Efficient Silicon Metasurfaces for Visible Light.* ACS Photonics, 2017. **4**(3): p. 544-551.

74. Zanotto, S., et al., *Metasurface Reconfiguration through Lithium-Ion Intercalation in a Transition Metal Oxide.* Advanced Optical Materials, 2017. **5**(2): p. 1600732.

75. Xiong, C., et al., *Active silicon integrated nanophotonics: ferroelectric BaTiO(3) devices.* Nano Lett, 2014. **14**(3): p. 1419-25.

76. Shalaev, M.I., et al., *High-Efficiency All-Dielectric Metasurfaces for Ultracompact Beam Manipulation in Transmission Mode.* Nano Lett, 2015. **15**(9): p. 6261-6.

77. Zia, R., *Dielectric metasurfaces: Transparent design.* Nat Nanotechnol, 2015. **10**(11): p. 913-4.

78. Wang, Q., et al., *Optically reconfigurable metasurfaces and photonic devices based on phase change materials.* Nature Photonics, 2015. **10**(1): p. 60-65.

79. Maria Papaioannou, E.P., João Valente, Edward TF Rogers and Nikolay I. Zheludev, *Two-dimensional control of light with light on metasurfaces.* Nature, 2016.

80. Valente, J., et al., *Reconfiguring photonic metamaterials with currents and magnetic fields.* Applied Physics Letters, 2015. **106**(11): p. 111905.

81. Ou, J.Y., et al., *Reconfigurable photonic metamaterials.* Nano Lett, 2011. **11**(5): p. 2142-4.

82. Ou, J.Y., et al., *An electromechanically reconfigurable plasmonic metamaterial operating in the near-infrared.* Nat Nanotechnol, 2013. **8**(4): p. 252-5.

83. Kim, Y., et al., *Reconfigurable chiroptical nanocomposites with chirality transfer from the macro- to the nanoscale.* Nat Mater, 2016. **15**(4): p. 461-8.

84. Landau, L.L., E, *On the theory of the dispersion of magnetic permeability in ferromagnetic bodies.* Phys. Z. Sowjetunion 1935. **8**: p. 153-169.

85. Gerrits, T.a.v.d.B., H. A. M. and Hohlfeld, J. and Bar, L. and Rasing, Th., *Ultrafast precessional magnetization reversal by picosecond magnetic field pulse shaping.* Nature, 2002. **418**(6897): p. 509--512.

86. Subkhangulov, R.R., et al., *Terahertz modulation of the Faraday rotation by laser pulses via the optical Kerr effect.* Nature Photonics, 2016. **10**(2): p. 111-114.